

CHAPTER 1

The Principles of Magnetic Resonance, and Associated Hardware

ANDREW WEBB*^a

^aC.J.Gorter Center for High Field MRI, Department of Radiology, Leiden University Medical Center, Leiden, The Netherlands

*E-mail: a.webb@lumc.nl

1.1 Introduction

The diversity of magnetic resonance (MR) experiments is enormous, ranging from simple one-dimensional proton nuclear magnetic resonance (NMR) spectroscopy through multi-dimensional multi-nuclear spectra to full three-dimensional magnetic resonance imaging (MRI) of morphology and function in animals and humans. Some examples of the types of data produced from different MR experiments are shown in Figure 1.1.

Despite the widely different information content of these data, the fundamental hardware systems for NMR spectroscopy (in both the liquid and solid states) and MRI (human and animal) are very similar. The basic components include the following:

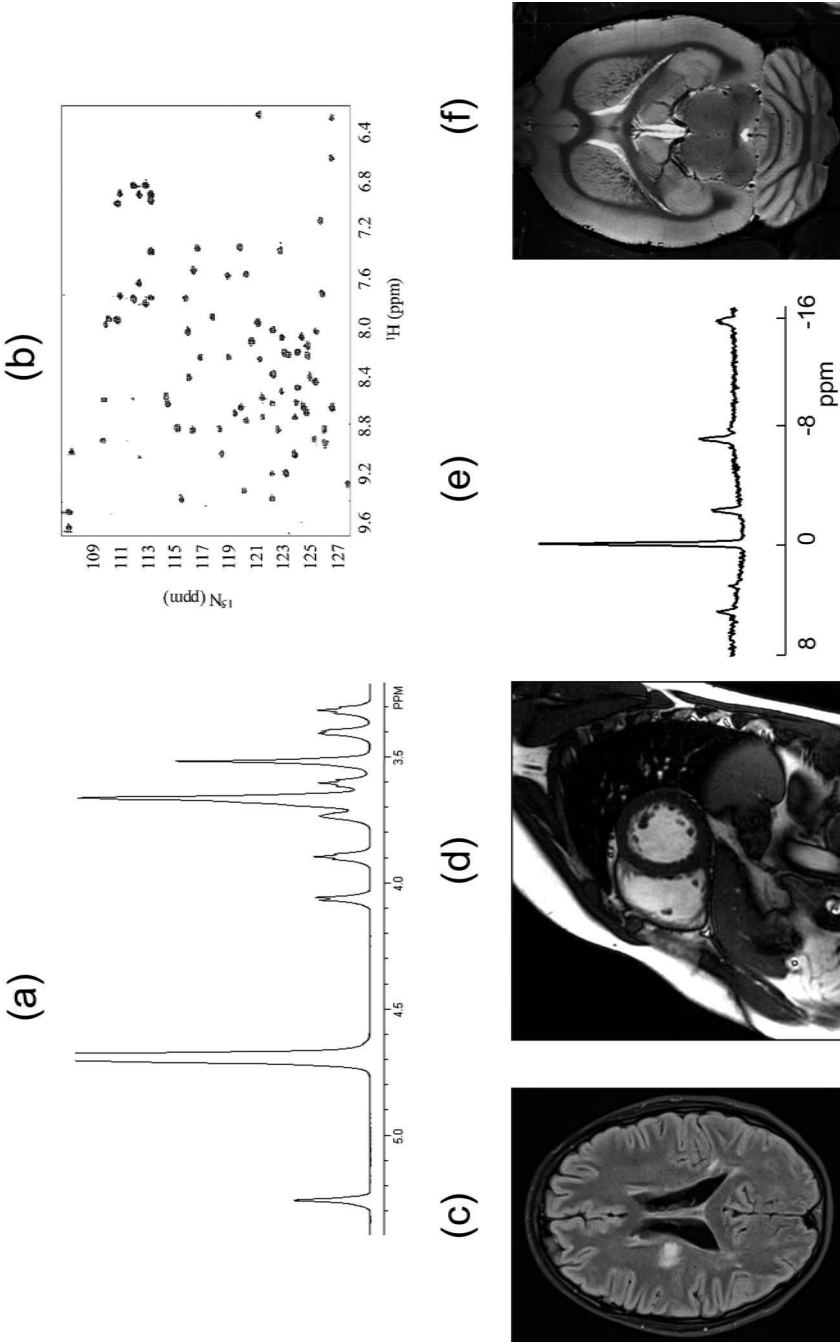


Figure 1.1 Examples of data produced from different magnetic resonance experiments. (a) One-dimensional proton NMR spectrum, (b) two-dimensional proton-nitrogen NMR spectrum, (c) proton image of the brain, (d) electrocardiogram-triggered proton image of the human heart, (e) phosphorus spectrum from the human calf muscle, and (f) proton image of a rat brain.

- (i) The magnet, which polarizes the nuclei and produces a net magnetization within the sample.
- (ii) The radiofrequency coil(s), which transmit pulses of electromagnetic (EM) energy into the sample and detect the precessing magnetization, which constitutes the MR signal.
- (iii) Magnetic field gradient coils, which induce a spatial dependence of the nuclear precession frequency and can be used for coherence order selection, measurements of diffusion, and MRI.
- (iv) Shim coils, which are used to produce as homogeneous a magnetic field as possible throughout the sample.
- (v) The receiver electronics and circuitry, which amplify, filter and digitize the MR signal for data storage and post-processing.

The physical arrangement of components (i) to (iv) is shown in Figure 1.2 for a vertical bore magnet.

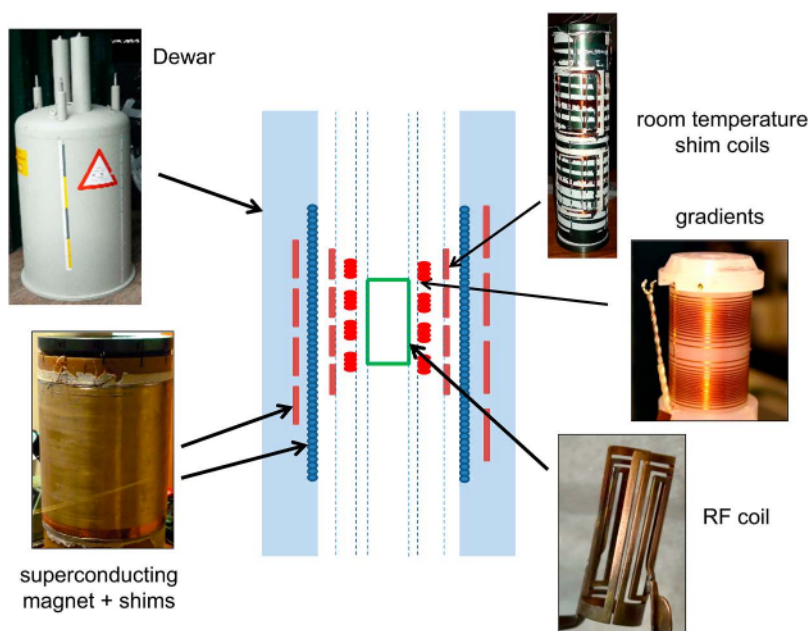


Figure 1.2 Schematic of the setup for high-resolution liquid-state NMR experiments. The vertical-bore superconducting magnet has a clear bore of either 89 mm (wide-bore) or 51 mm (narrow-bore). Sets of superconducting shim coils are embedded within the cryostat. Additional room temperature shims are located inside the magnet bore. The next level inwards comprises the magnetic field gradient set, which may consist of one- or three-axis gradients. The innermost structure is the RF coil containing the NMR sample.

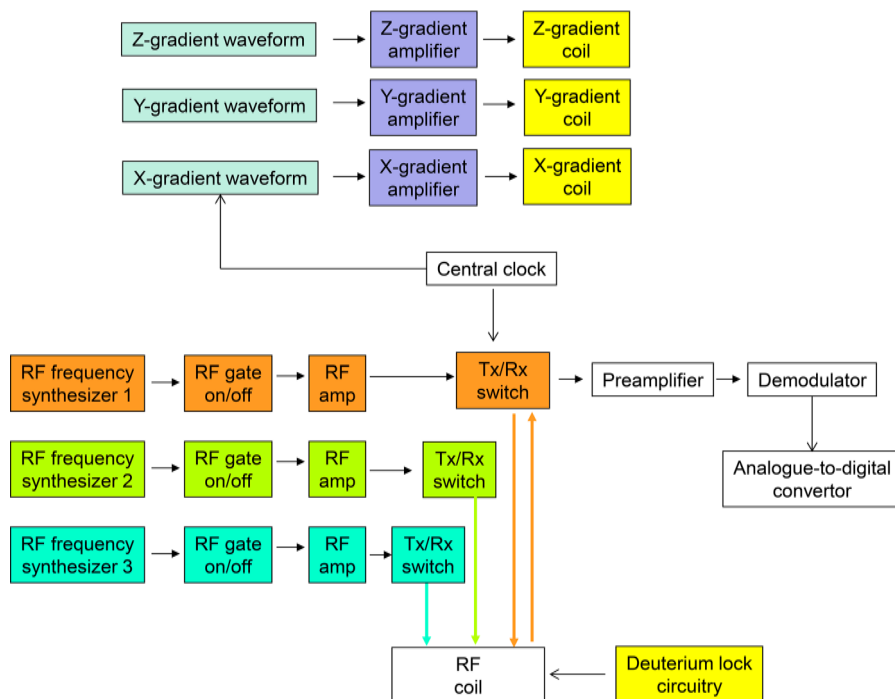


Figure 1.3 Block diagram of a generic MR system. The timing of RF pulses, gradient pulses, and data acquisition are all tied to a central clock. For high-resolution NMR there are typically three or four different frequency channels (in addition to the lock channel) transmitting RF pulses, whereas for MRI usually only a proton channel is present. In high-resolution NMR a single receive coil is used: in contrast, for MRI there are usually multiple receiver coils and associated receive channels, with 32 being a typical number for commercial systems.

In addition, there are a series of electronic components used to switch the gradients on and off, to produce high power RF pulses, and to amplify and digitize the signal. A simplified block diagram of a generalized MR system is shown in Figure 1.3.

Table 1.1 gives an idea of the characteristics and performance of components in typical commercial NMR and MRI systems. The system performances of each of the components in the table are explained in greater detail in the relevant sections throughout the book.

In the following sections in this chapter the basic phenomena involved in magnetic resonance are explained briefly, with links to the relevant system hardware. There are a large number of MR books dealing with the basic theory of high-resolution liquid-state NMR,^{1–5} solid-state NMR^{6–9} and MRI,^{10–13} and readers are advised to consult these tomes for much more in-depth analyses of different aspects of basic MR theory.

Table 1.1 Characteristics of the magnet, gradients, and RF coils in commercial systems.

	NMR	MRI	MRI
Static magnetic field	4.7–23.5 tesla	Human 1.5–9.4 tesla	Animal 4.7–21.1 tesla
Proton frequency	200 MHz–1 GHz	63.8–400 MHz	200–900 MHz
Gradient strength	500 ^a mT m ⁻¹	40–80 ^b mT m ⁻¹	1 T m ⁻¹ (6 cm i.d.) 750 mT m ⁻¹ (9 cm i.d.) 450 mT m ⁻¹ (12 cm i.d.)
RF coil diameter	1.3–20 mm	10–60 cm	10–60 mm
RF amplifier power	1 kW	30 kW	4 kW
Shortest pulse	~1 μs	~10–50 μs	5–10 μs

^aSingle axis diffusion gradients can reach ~25 T m⁻¹.

^b300 mT m⁻¹ for specialized systems for the human-connectome project.^{28,29}

1.2 The Superconducting Magnet and Nuclear Polarization

The role of the magnet is to polarize the nuclei to produce a net magnetization within the sample. For NMR spectroscopy and MRI, almost all magnets are superconducting. The magnetic field should be temporally stable and homogeneous to within parts-per-billion (ppb) throughout the sample. Most magnets are actively shielded, *i.e.* the fringe field does not extend significantly outside the physical dimensions of the magnet itself. Magnet design is considered in detail in Chapter 2 of this book, as well as Appendix 1A at the end of this chapter.

All nuclei with an odd atomic weight and/or an odd atomic number possess a fundamental quantum mechanical property termed “spin” and are termed “spin-active” or “NMR-active”. The most important spin-active nuclei include ¹H, ¹³C, ¹⁵N, ²³Na, ¹⁷O, ³¹P and ²H. Notably *spin-inactive* are nuclei such as ¹⁶O and ¹²C. Considering the proton as the simplest example, the property of spin can be viewed as the proton spinning around an internal axis of rotation giving it a certain value of angular momentum (P). Since the proton is a charged particle, this rotation results in a magnetic moment (μ). This magnetic moment produces an associated magnetic field, which has a configuration similar to that of a bar magnet. The magnitude of P is quantized in terms of the nuclear spin quantum number (I):

$$|\vec{P}| = \frac{\hbar}{2\pi} [I(I+1)]^{1/2} \quad (1.1)$$

where \hbar is Planck’s constant (6.63×10^{-34} Js). In the following analysis a spin 1/2 nucleus ($I = 1/2$) is considered, corresponding to ¹H, ¹³C, ¹⁵N, and ³¹P in the previous list. In this case:

$$|\vec{P}| = \frac{\hbar}{2\pi} \frac{\sqrt{3}}{2} \quad (1.2)$$

The magnitudes of the magnetic moment and the angular momentum of the proton are related by:

$$|\vec{\mu}| = \gamma |\vec{P}| = \frac{\gamma \hbar}{2\pi} [I(I+1)]^{\frac{1}{2}} \tag{1.3}$$

where γ is the nuclear gyromagnetic ratio, and has a specific value for different nuclei, with protons having the highest γ (with the exception of tritium). For protons therefore:

$$|\vec{\mu}| = \frac{\gamma \hbar \sqrt{3}}{4\pi} \tag{1.4}$$

μ contains three components (μ_x, μ_y and μ_z), each of which can have any value within the conditions governed by eqn (1.4): this situation is shown in Figure 1.4(a). However, in the presence of a strong magnetic field, B_0 , μ_z is quantized with values given by:

$$\mu_z = \frac{\gamma \hbar}{2\pi} m_1 \tag{1.5}$$

where m_1 is the nuclear magnetic quantum number, and can take values $I, I - 1 \dots -I$. In the case of a proton, $m_1 = \pm 1/2$ and so:

$$\mu_z = \pm \frac{\gamma \hbar}{4\pi} \tag{1.6}$$

The orientation of μ with respect to B_0 is shown in Figure 1.4(b). The interaction of the static magnetic (B_0) field with μ_z results in Zeeman splitting, producing two energy levels: one in which μ_z aligns parallel to B_0 (the lower energy state) and the other anti-parallel (the higher energy state).

The net magnetization, M_0 , of a sample containing N_s protons is proportional to the difference in populations between the two energy levels, which is dictated by Boltzmann's equation:

$$M_0 = \sum_{n=1}^{N_s} \mu_{z,n} = \frac{\gamma \hbar}{4\pi} (N_{\text{parallel}} - N_{\text{anti-parallel}}) = \frac{\gamma^2 \hbar^2 B_0 N_s}{16\pi^2 kT} \tag{1.7}$$

Eqn (1.7) shows that the net polarization of a sample is proportional to the strength of the main magnetic field. However, since the energy difference between the two levels is very small, so is the population difference. For example, at an operating magnetic field of 11.7 tesla for every one million protons, there is a population difference of only ~40 protons between the parallel and anti-parallel orientations.

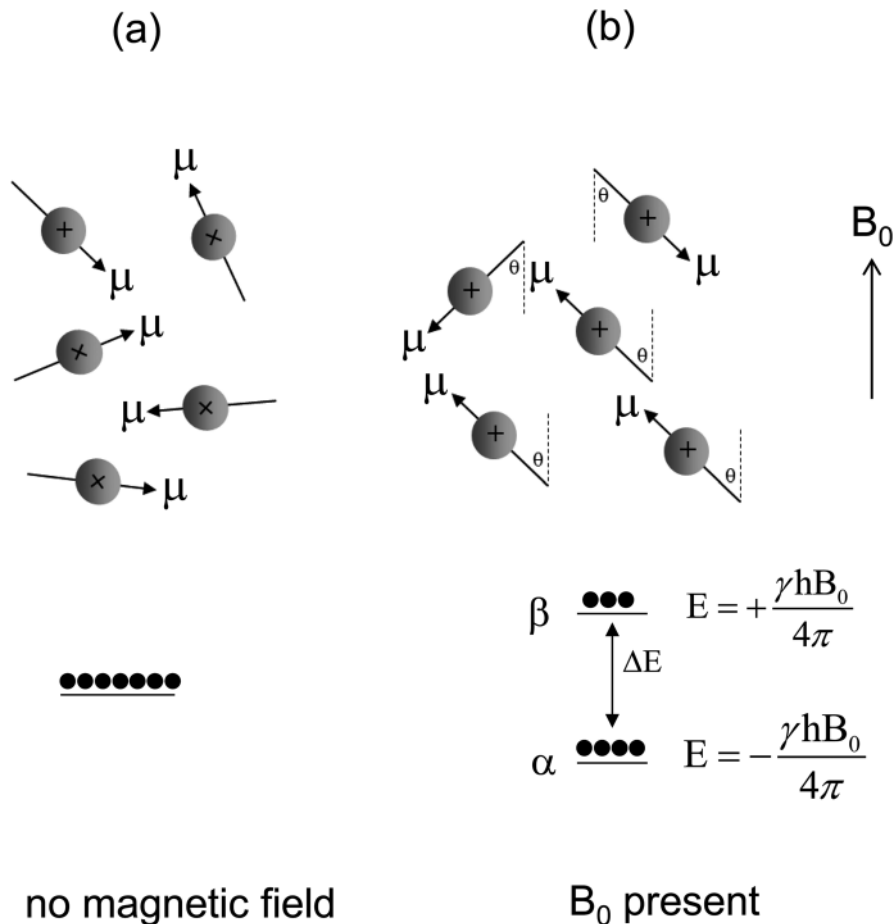


Figure 1.4 (a) In the absence of a magnetic field μ lies in a random direction and the nuclei occupy a single energy level. (b) When a static magnetic field is applied, μ_z becomes quantized at an angle θ of 54.7° with respect to B_0 . Parallel (α) and anti-parallel (β) orientations correspond to two energy levels, with a difference $\Delta E = \gamma\hbar B_0/2\pi$. A greater number of nuclei occupy the lower energy, parallel state.

1.3 The Transmitter Coil to Generate Radiofrequency Pulses

In order to detect an MR signal, energy must be applied to the nuclear spin system to stimulate transitions between the two energy levels. A pulse of EM energy is applied at the specific resonance frequency (f_0), which corresponds to the energy difference between the two levels *via*:

$$hf_0 = \Delta E = \frac{\gamma\hbar B_0}{2\pi} \tag{1.8}$$

The resonance frequency in Hz, or resonance angular frequency (ω_0) in radians per second, is therefore given by:

$$f_0 = \frac{\gamma B_0}{2\pi}, \omega_0 = \gamma B_0 \quad (1.9)$$

The pulsed EM wave consists of both magnetic and electric field components, and it is the *magnetic* component that interacts with the nuclear magnetization. The EM energy, termed a radiofrequency (RF) pulse, is transmitted *via* an RF coil. As shown in Figure 1.5, the magnetic field component, B_1^+ , of the EM wave from the RF coil must be created in a direction *perpendicular* to B_0 in order to interact with the magnetization.

Using classical mechanics, the action of the RF pulse applied along one axis produces a torque perpendicular to that axis. As shown in Figure 1.5(b), the angle α by which the magnetization is rotated is proportional to the product of the strength of the applied RF field and the time, τ_{B_1} , for which it is applied.

$$\alpha = \gamma B_1^+ \tau_{B_1} \quad (1.10)$$

After application of an RF pulse with tip angle α about the x -axis, the net magnetization can be expressed as three different vectors.

$$M_z = M_0 \cos \alpha, M_x = 0, M_y = M_0 \sin \alpha \quad (1.11)$$

The geometric design of the RF coil is determined by the requirement that the B_1^+ field produced by the coil must be perpendicular to B_0 . There are a large number of different geometries, which are discussed in detail in Chapter 3. One example, widely used in high-resolution liquid-state NMR, is the “saddle” coil, shown in Figure 1.6. The long axis of the coil is coincident with B_0 , and current flowing through the copper conductor produces a B_1^+ field with the required orientation. The RF coil is tuned and impedance matched to 50 Ω at the Larmor frequency for high efficiency. The RF coil may be tuned to more than one frequency, as also discussed in Chapter 3.

Power to the RF coil is supplied by an RF amplifier, the general specifications of which include:

- (i) Amplifiers for liquid-state and solid-state NMR experiments must be able to produce pulses as short as 1 μ s, with accurate and reproducible shape, at frequencies up to \sim 1 GHz. In solid-state NMR applications, very high power pulses with a very high duty cycle may be used for proton decoupling.
- (ii) In the case of MRI, up to 30–60 kW of power must be available without the performance varying over time owing to any component heating, as well as the amplifiers being capable of high duty cycles for RF-intensive sequences, such as turbo spin-echoes.

The design of RF amplifiers is described in detail in Chapter 6.

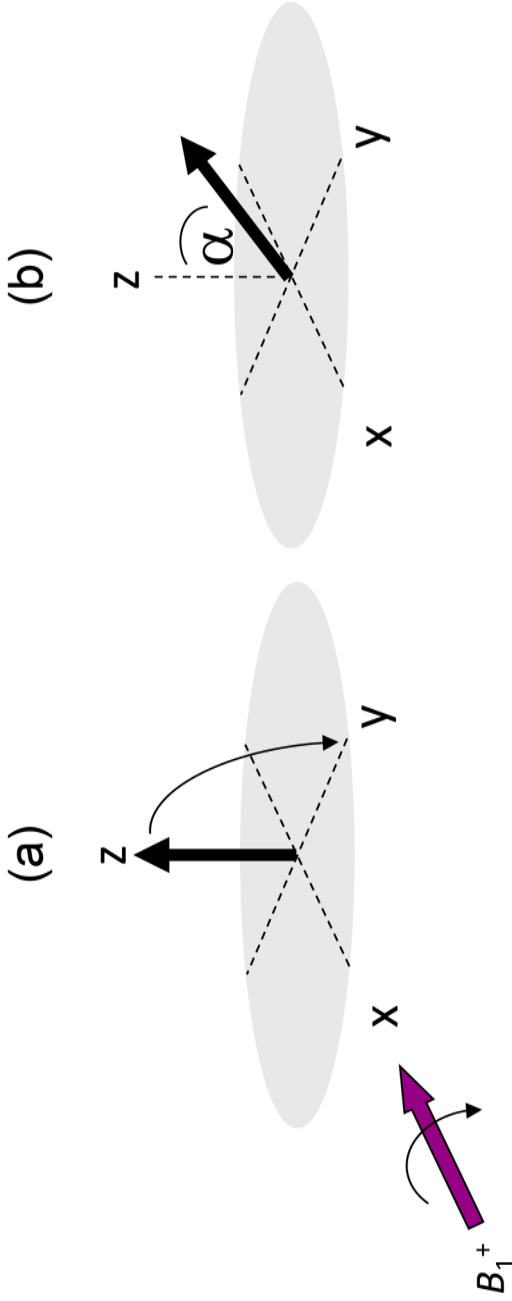


Figure 1.5 (a) The effect of an RF pulse on the net magnetization is to rotate the magnetization about the axis along which B_1^+ is applied.
(b) The angle of rotation α is given by eqn (1.10).

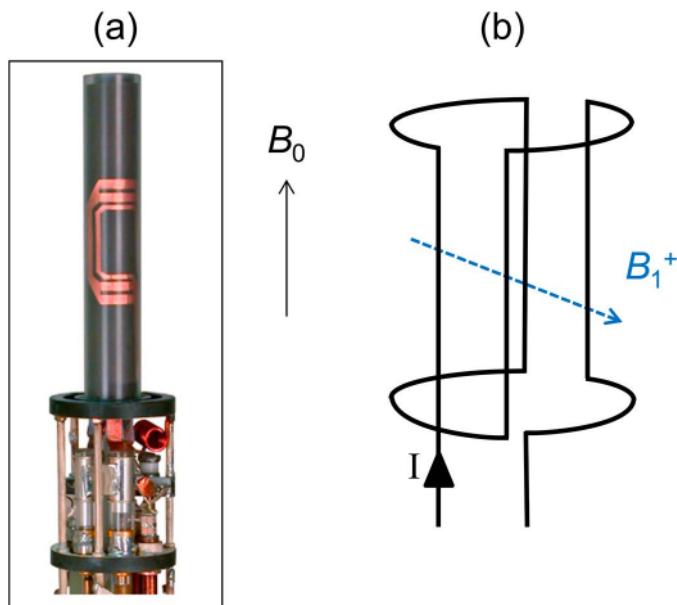


Figure 1.6 (a) Photograph of a saddle coil, formed of an etched copper substrate, used for high-resolution liquid-state NMR. The electrical circuitry used for tuning and impedance matching is situated below the coil. The sample is placed in the centre of the coil. (b) Current I flowing through the coil produces a B_1 field that is perpendicular to B_0 .

1.4 Precession

When the RF pulse is turned off, the component of magnetization in the transverse plane precesses around B_0 , as shown in Figure 1.7(a). The precession frequency, $\omega_{\text{precession}}$, is exactly the same as the frequency of irradiation:

$$\omega_{\text{precession}} = \omega_0 = \gamma B_0 \quad (1.12)$$

The concept of a rotating reference frame is very useful in analyzing the behaviour of the net magnetization, and is shown in Figure 1.7(b). The rotating reference frame ($x'y'$) is defined as rotating around B_0 at an angular frequency ω_0 .

In fact, the exact precession frequencies of different nuclei within a molecule are determined by two other factors, chemical shift and scalar coupling, which are outlined in the following sections.

1.4.1 Chemical Shift

The term “chemical shift” refers to the fact that protons in different chemical environments within a molecule resonate at slightly different frequencies: their precession frequencies are *shifted* (with respect to a reference, discussed below) with the magnitude of the shift depending on their particular *chemical* environment. The cause of this shift is that the exact magnetic field

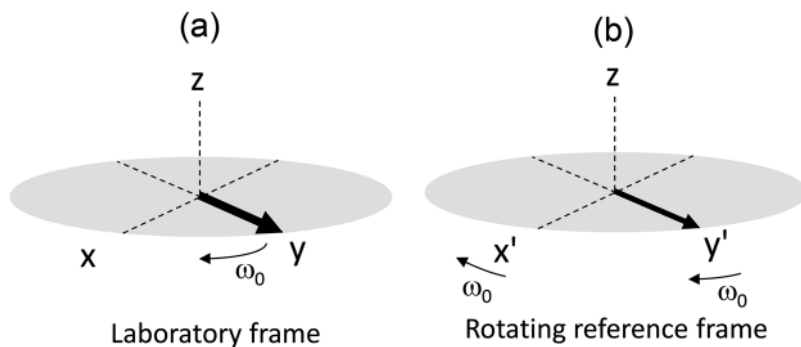


Figure 1.7 (a) Immediately after a 90° pulse about the x -axis, the magnetization lies along the y -axis, and starts to precess at a frequency $\omega_{\text{precession}}$, given by eqn (1.12). (b) In the rotating reference frame the magnetization vector appears static.

experienced by each proton in the molecule is slightly lower than B_0 owing to the shielding effects of the electron cloud surrounding each proton. Electrons have a magnetic moment, which is opposite in sign to that of the proton, and so the effective magnetic field experienced by the proton is reduced. As an example, consider the lactic acid molecule shown in Figure 1.8. There are four different proton groups (CH_3 , CH , OH , COOH) in this molecule: each of these proton groups has a slightly different precession frequency since they experience a slightly different magnetic field. The effective magnetic field, B_{eff} , experienced by a proton is given by:

$$B_{\text{eff}} = B_0(1 - \sigma) \quad (1.13)$$

where σ is called the shielding constant, and is related to the electronic environment surrounding the nucleus. The resonant frequency of the proton is given by:

$$\omega = \gamma B_{\text{eff}} = \gamma B_0(1 - \sigma) \quad (1.14)$$

One of the main factors that determines the value of σ is the electronegativity of the atoms connected to the protons: the proton in an $-\text{OH}$ group has a lower shielding constant than those in a $-\text{CH}_2-$ group since oxygen is more electronegative than carbon and pulls electrons away from the proton, thus reducing the shielding. The resonant frequency of the proton of an $-\text{OH}$ group is therefore higher than that of the protons in a $-\text{CH}_2-$ group. The chemical shift (δ), in units of parts-per-million (ppm), is defined as:

$$\delta(\text{ppm}) = 10^6 \frac{f - f_{\text{ref}}}{f_{\text{ref}}} \quad (1.15)$$

where f_{ref} is the resonant frequency of the protons in tetramethylsilane (TMS), which acts as a reference for proton NMR spectra. Figure 1.9 shows approximate chemical shift ranges for protons in different chemical

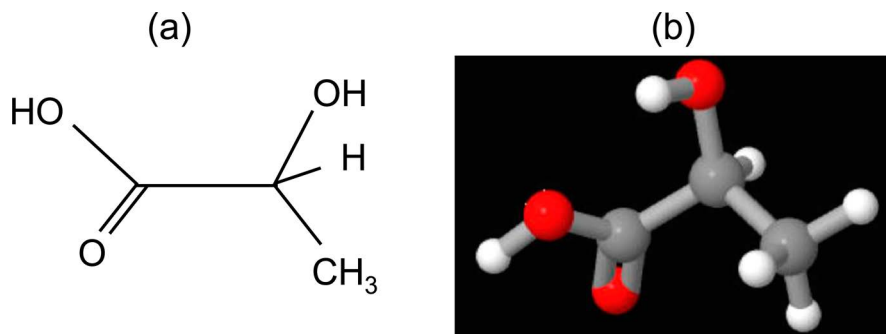


Figure 1.8 (a) Chemical structure of a lactic acid molecule. (b) Ball-and-stick model of the lactic acid molecule with oxygens shown in red, protons in white and carbons in gray.

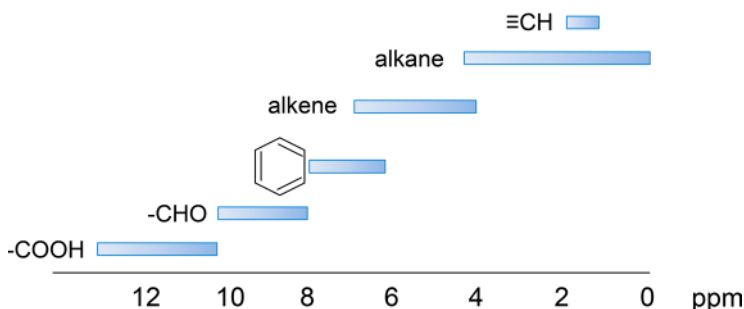


Figure 1.9 The range of proton chemical shifts for different chemical moieties.

environments. For the lactic acid molecule, the order of resonance frequencies is: $\text{CH}_3 < \text{CH} < \text{OH} < \text{COOH}$.

1.4.2 Scalar Coupling

Consider the protons in the molecule shown in Figure 1.10. There are three chemically distinct protons (H_A , H_B , and H_C), which have three different chemical shifts and corresponding resonant frequencies. However, there is also an interaction between the two protons H_A and H_B , which are separated by three chemical bonds (H_A -to-C-to-C-to- H_B). The magnetic field experienced by H_A depends upon whether H_B is in the α (parallel) or β (anti-parallel) state, and *vice versa*: this phenomenon is termed scalar coupling. Therefore, there are four different energy levels for this coupled two-proton system: $\alpha\alpha$, $\alpha\beta$, $\beta\alpha$, and $\beta\beta$, as shown in Figure 1.10(b). The exact value of the scalar coupling constant J depends upon a number of

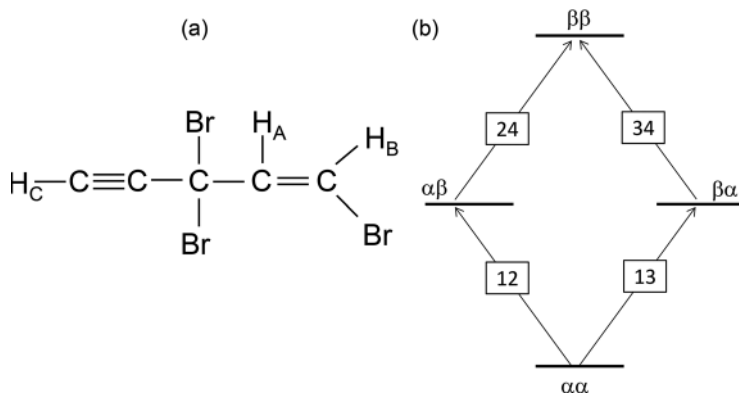


Figure 1.10 (a) A chemical molecule with three different protons. H_A and H_B are scalar coupled, whereas H_C is not coupled. (b) Energy level diagram for the coupled H_A and H_B protons.

different factors, including the particular type of chemical bond (single, double or triple bond), as well as the angle subtended between the C–H bonds (the Karplus angle), but in general the values are between 1 and 7 Hz. The greater the number of bonds between the protons the weaker the coupling, and so for the molecule in Figure 1.10(a) there is effectively no coupling between H_A and H_C since there are five chemical bonds between the protons.

For the coupled H_A – H_B system, the four different transition energies corresponding to the energy level diagram in Figure 1.10(b) are given by:

$$\begin{aligned}\omega_{12} &= \omega_A - \frac{1}{2}J_{AB}, \omega_{34} = \omega_A + \frac{1}{2}J_{AB} \\ \omega_{13} &= \omega_B - \frac{1}{2}J_{AB}, \omega_{24} = \omega_B + \frac{1}{2}J_{AB}\end{aligned}\quad (1.16)$$

Figure 1.11 shows the evolution of the precessing magnetization for the three different protons. From Figure 1.9 the chemical shift of H_C has the lowest value, followed by H_A and the highest value for H_B . H_C precesses at a single frequency, whereas protons H_A and H_B are “split” into two frequencies by the scalar coupling.

1.4.3 Relaxation Processes

The final effect that must be considered in terms of the precession of the net magnetization is relaxation. After the RF pulse has been turned off, each of the magnetization components M_z , M_x and M_y returns to their thermal equilibrium values, with the time-evolution determined by specific time-constants.

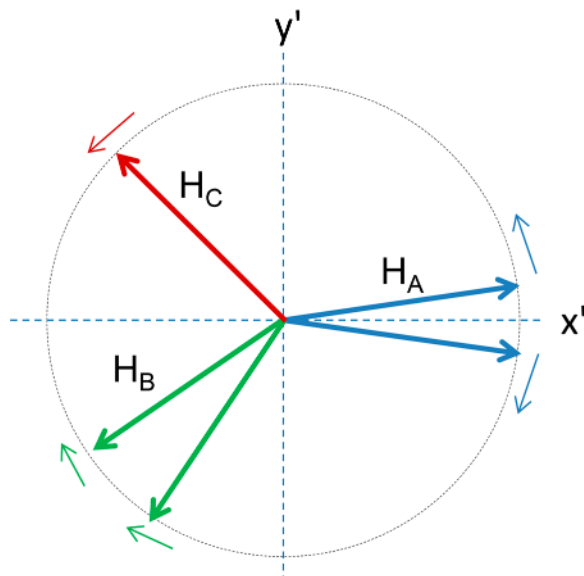


Figure 1.11 Evolution of the magnetization in the molecule shown in Figure 1.10 from the combined effects of chemical shift and scalar coupling. The rotating reference frame ($x'y'$) frequency is set to the chemical shift of H_A .

The time-evolutions of M_z , M_x and M_y are characterized by differential equations known as the Bloch equations:¹⁴

$$\begin{aligned}\frac{dM_x}{dt} &= \gamma M_y \left(B_0 - \frac{\omega}{\gamma} \right) - \frac{M_x}{T_2} \\ \frac{dM_y}{dt} &= \gamma M_z B_1 - \gamma M_x \left(B_0 - \frac{\omega}{\gamma} \right) - \frac{M_y}{T_2} \\ \frac{dM_z}{dt} &= -\gamma M_y B_1 - \frac{M_z - M_0}{T_1}\end{aligned}\quad (1.17)$$

The return of M_z to its equilibrium value of M_0 is governed by the spin-lattice (T_1) relaxation time, and the return of M_x and M_y to their thermal equilibrium value of zero by the spin-spin (T_2) relaxation time. It should be noted that the relative values of T_1 and T_2 can be very different for different types of sample, but T_1 is always *greater or equal* to T_2 . For non-viscous liquids used in high-resolution NMR, the values of T_1 and T_2 are very similar. In contrast, in solid samples T_2 can be up to six orders shorter than T_1 , and for human MRI the T_2 of many soft tissues is between one and two orders of magnitude smaller than T_1 .

Solving the Bloch equations for the M_x and M_y components of magnetization gives:

$$M_y(t) = M_y(t=0)e^{-t/T_2}, \quad M_x(t) = M_x(t=0)e^{-t/T_2}\quad (1.18)$$

Therefore, the precessing magnetization vectors shown in Figure 1.11 decay exponentially as a function of time. In practice, there is an addition term that gives rise to the decay of transverse magnetization, which is termed “inhomogeneous line-broadening” and has a time-constant of T_2^+ . This term arises from spatial inhomogeneities in the magnetic field within the sample as-a-whole, and can arise from the magnet itself or more commonly with an inhomogeneous sample. The overall relaxation time for transverse magnetization is termed T_2^* , which is given by:

$$T_2^* = \frac{T_2 T_2^+}{T_2 + T_2^+} \quad (1.19)$$

The return of M_z to its thermal equilibrium value of M_0 is governed by the T_1 relaxation time:

$$M_z(t) = M_z(t=0) + (M_0 - M_z(t=0)) \left(1 - e^{-\frac{t}{T_1}} \right) \quad (1.20)$$

1.5 The Receiver Coil for Detecting the MR Signal

In high-resolution NMR experiments, the same RF coil used to transmit the RF pulses is also used to detect the MR signal. In contrast, in MRI experiments a large number of small coils are typically used to receive the signal, with (usually) a single large coil used to transmit the RF pulses. For simplicity, and without losing generality, Figure 1.12(a) shows the case relevant to

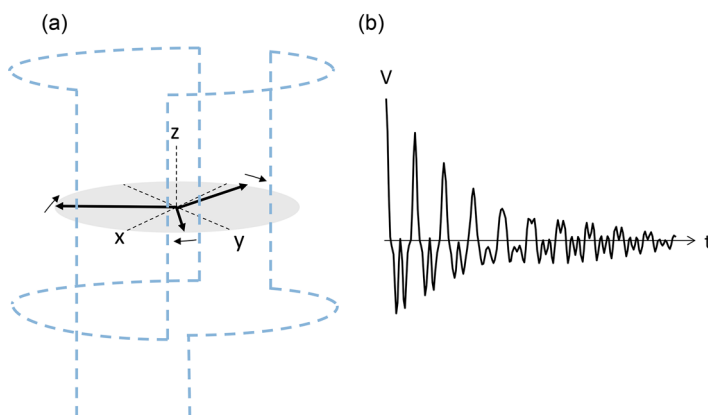


Figure 1.12 (a) Detection of the MR signal occurs *via* the voltage induced across the terminals of an RF coil by the time-varying magnetic flux produced by the precessing magnetization. (b) The induced voltage as a function of time, incorporating chemical shift and scalar coupling, as well as T_2^* relaxation.

high-resolution NMR in which the saddle coil shown in Figure 1.6 is used as the receiver coil. The time-varying magnetic field produced by the precession of the magnetization vectors results in a voltage being induced in this receiver coil. The induced voltage, V , is given by Faraday's law and is proportional to the rate-of-change of magnetic flux:

$$V = -\frac{\partial\phi(t)}{\partial t} = -\frac{\partial}{\partial t} \int_{\text{sample}} \frac{B_1}{I} \cdot M_{xy} \, dr \quad (1.21)$$

where the coil sensitivity is defined as B_1/I , *i.e.* the B_1 field produced per unit applied current. At higher strengths of the B_0 field, the protons precess at a higher frequency, the value of $d\phi/dt$ increases, and so the detected MR signal is higher.

The time-domain signal is shown in Figure 1.12(b). Based on the previous sections the signal contains a number of different frequencies owing to chemical shift and the effects of scalar coupling, and decays exponentially as a function of time. The time-domain signal is usually referred to as the free induction decay (FID).

1.6 The Receiver: Signal Demodulation, Digitization and Fourier Transformation

The analogue time-domain signal shown in Figure 1.12(b) must be converted into a digital signal so that it can be stored and processed. Typically, the magnitude of the signal is on the order of millivolts or even lower, which means that it cannot be digitized directly with a high dynamic range by a commercial analogue-to-digital converter (ADC). It must first pass through the MR receiver, which is covered in detail in Chapter 7 and so only a brief overview is given here.

1.6.1 Receiver Electronics

A block diagram of the electronic circuits in the receiver is shown in Figure 1.13. The signal first passes through a low-noise preamplifier, with a typical gain factor of 20–30 dB and noise figure ~ 0.5 dB. Commercial ADCs used in MR have a maximum input voltage of 5 volts, with resolution of 16 bits, and so the voltage should be amplified to close to 5 volts before being digitized, otherwise the full dynamic range of the ADC is not utilized.

High-resolution ADCs cannot sample at the very high frequencies associated with MR, and so it is necessary to demodulate the signal to reduce the sampling rate in order to take advantage of the high dynamic range. The first demodulation step uses two phase sensitive detectors (PSDs), with the inputs to the two PSDs phase shifted by 90° to produce real and imaginary

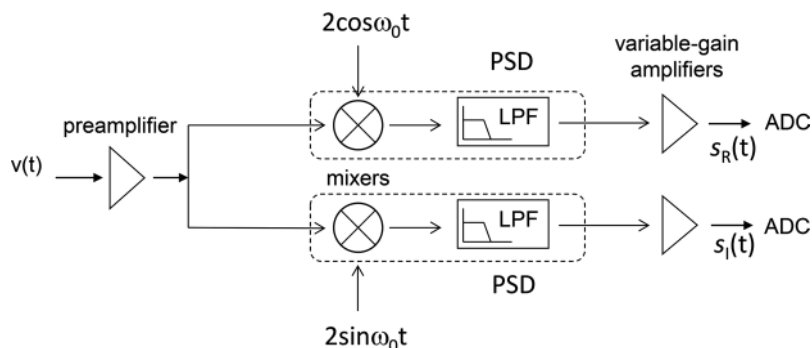


Figure 1.13 Block diagram of the individual components in an MR receiver.

outputs centred at a lower intermediate frequency, ω_{IF} . Each PSD contains a mixer and low pass filter, with the mixer effectively acting as a signal multiplier. The output of the mixer has frequency components at $(\omega_0 + \omega_{IF})$ and $(\omega_0 - \omega_{IF})$: the low pass filter removes the higher frequency components. The real, $s_R(t)$, and imaginary, $s_I(t)$, components of the signal pass through a second amplification stage and are digitized using separate ADCs. In practice, digital sampling is now common in both NMR and MRI,¹⁵ and is discussed further in Chapter 7.

1.6.2 Signal Processing

In NMR experiments, after the signal has been digitized and stored, it is Fourier transformed into the frequency domain (for imaging experiments, covered later in this chapter, the transformation is a multi-dimensional inverse Fourier transform). The frequency-domain signal has both real, $S_R(f)$, and imaginary, $S_I(f)$, components given by:

$$S_R(f) + S_I(f) \propto M_0 \left(\frac{T_2^*}{1 + (2\pi T_2^* f)^2} - j \frac{(T_2^*)^2 2\pi f}{1 + (2\pi T_2^* f)^2} \right) \quad (1.22)$$

The real part of the frequency-domain signal, $S_R(f)$, is termed the absorption-mode spectrum, as shown in Figure 1.14. Each line in the spectrum is described by a Lorentz function with a full-width-half-maximum (FWHM) given by $(\pi T_2^*)^{-1}$. The imaginary component of the frequency-domain signal is termed the dispersion-mode spectrum, as also shown in Figure 1.14. The real part of the spectrum is displayed after the phase of the spectra is adjusted to account for the finite delay between the RF pulse being switched off and the start of data acquisition. Frequency independent (zero-order) and frequency-dependent (first-order) phasing are applied so that the real part of the spectrum is completely absorptive.

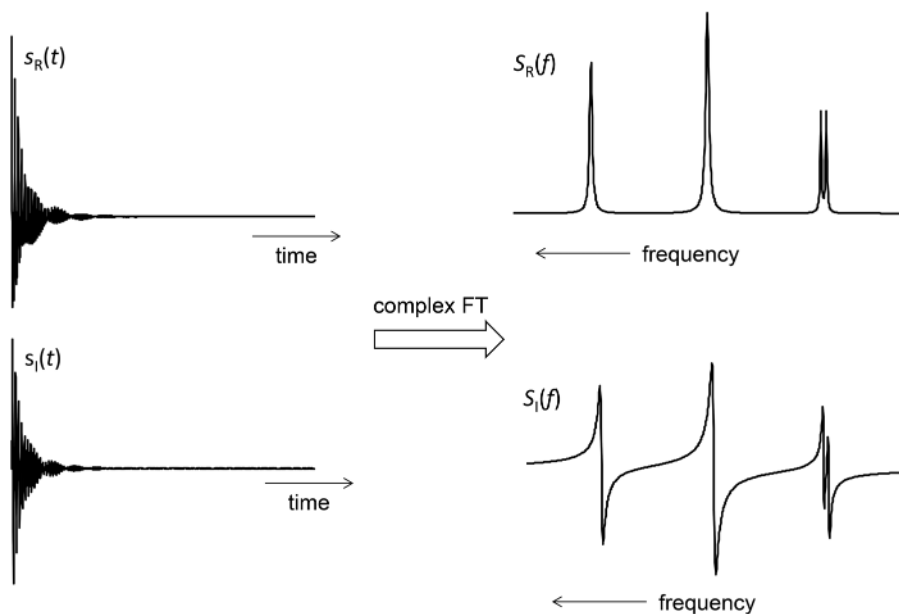


Figure 1.14 Fourier transformation of the complex time-domain digitized signal gives an absorption spectrum (top) and a dispersion spectrum (below).

1.7 Shim Coils

Despite every effort to construct a magnet that produces a completely homogeneous static field throughout the entire sample, this is impossible to achieve in practice. Finite mechanical tolerances in winding and placement of the superconducting wires, and material imperfections within the superconducting wire itself result in a small degree of spatial variation of the B_0 field. Indeed, it is theoretically only possible to produce a completely homogeneous field with an infinitely long magnet, as covered in Chapter 2. Furthermore, unless the sample is a pure liquid, the different magnetic susceptibilities of components within the sample, and in particular the boundaries between these components, produce distortions in the magnetic field: this is the case particularly for MRI experiments in animals or humans, as described in Chapter 4.

In order to counteract this sample-dependent inhomogeneity in the static magnetic field, it is necessary to introduce “shim coils”, which are discussed in more detail in Chapter 4. These are “correction” coils, through which current can be passed to produce a spatially-varying compensatory magnetic field for the particular sample being studied. There are two different types of shim coils: (i) superconducting shim coils, which are situated in the cryostat of the magnet, as shown in Figure 1.2, and which are adjusted only during magnet installation, and (ii) room-temperature shims, which are normally placed on the inside of the magnet bore. In high-resolution NMR there may be up to thirty different shim coils through which current can be passed. The reason for such a high number is that it is essential to obtain narrow linewidths in high-resolution NMR

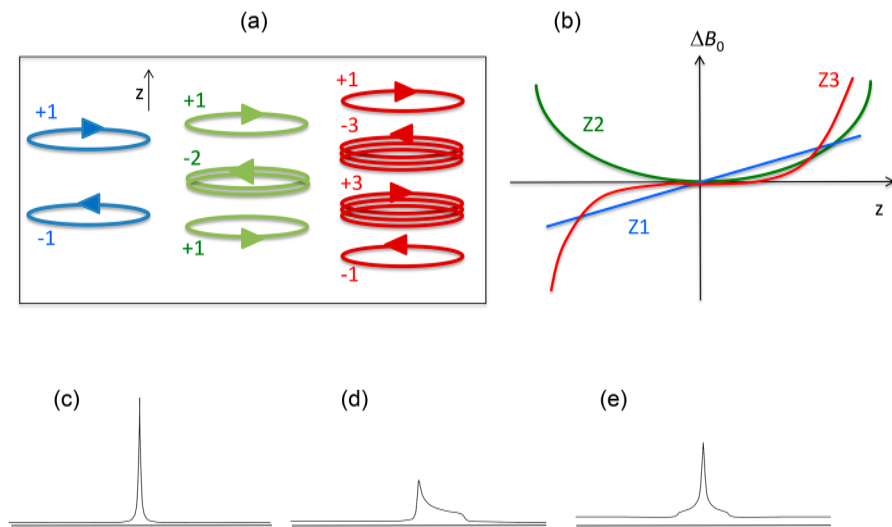


Figure 1.15 (a) Wire geometries for Z1, Z2 and Z3 shim coils with the appropriate relative current values and directions provided by the individual shim DC power supplies. (b) The spatial variation in magnetic field in the z -direction for each of the Z1, Z2 and Z3 shim coils. (c) A spectrum showing a well-shimmed line shape. (d) A spectrum showing low-field asymmetry produced by a sub-optimal value of the Z2 shim. (e) A spectrum displaying a symmetric broad baseline produced by a sub-optimal value of the Z3 shim.

spectroscopy in order to separate the resonances from protons in similar chemical environments. In MRI there are far fewer shim coils since: (i) imaging is inherently less sensitive than spectroscopy to B_0 field inhomogeneities, (ii) the effect of the shims is less since they are situated a much greater distance away from the sample than in high-resolution NMR, and (iii) the intrinsic inhomogeneities produced by the sample are much greater.

The geometry of the shim coils is designed to produce different spatial variations in the magnetic field. Figure 1.15(a) shows examples of three sets of shim coils used to produce different spatial compensations to the magnetic field, Figure 1.15(b), as a function of location in the z -direction. The effects of mis-setting the shim currents are also shown in Figure 1.15.

Optimization of the currents through the shim coils can be performed in two different ways. In one method, the real component of the deuterium lock signal is monitored, covered later in Section 1.9, in the other method magnetic field gradients are used, as described in Section 1.8.4.

1.8 Gradient Coils

Magnetic field gradient coils, a term usually shortened to simply “gradient coils”, are designed to produce a linear dependence of the effective magnetic field on spatial position. They consist of shaped conductors (wires or thin sheets) through which current passes to produce the gradient field. In

high-resolution NMR probes, a single z -axis gradient coil is usually integrated into the RF probe, although three-axis gradients can also be present. For MRI, three independent orthogonal sets of gradient coils are present, each controlled by independent gradient amplifiers.

Since only the z -component of the magnetic field (B_z) interacts with the proton magnetic moments, it is the spatial variation of B_z that is relevant. The magnetic field gradients are designed to be linear over the sample, *i.e.*:

$$\frac{\partial B_z}{\partial z} = G_z \quad (1.23)$$

Figure 1.16 shows a plot of magnetic field *vs.* spatial position for a gradient applied along the z -axis.

When the gradient is switched on by passing current through the coil, the magnetic field B_z becomes a function of z position and is given by:

$$B_z = B_0 + zG_z \quad (1.24)$$

where G_z has units of tesla (T) per metre. The corresponding precession frequencies (ω_z) of the protons, in the rotating frame, are given by:

$$\omega_z = \gamma z G_z \quad (1.25)$$

Details on gradient coil design, as well as the gradient amplifiers, are covered in Chapter 5. Gradient coils are used for many purposes in MR, the following being the most common:

- (i) Dephasing or “crushing” of unwanted transverse magnetization.
- (ii) Coherence selection in multiple quantum coherence experiments.¹⁶

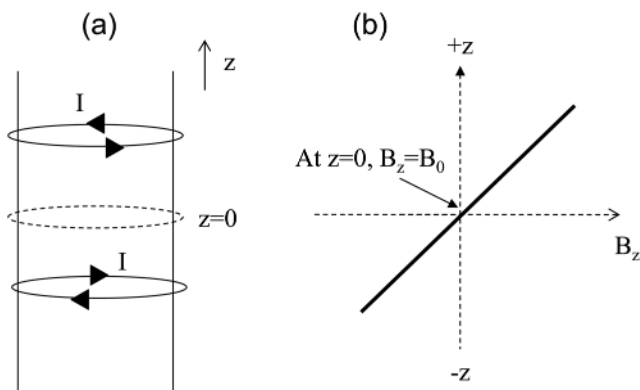


Figure 1.16 A linear gradient in the z -direction can be produced by two sets of loops of wire (a), each one carrying current in the opposite direction. (b) Midway between the loops, at $z = 0$, the additional magnetic field from the two sets of loops cancels out, and the magnetic field experienced by the nuclei is B_0 .

- (iii) Measurements of apparent diffusion coefficients of liquid samples,¹⁷ or tissues in MRI.¹⁸
- (iv) Rapid optimization of shim currents for high-resolution NMR and MRI.
- (v) Spatial localization in MRI^{19,20} and localized *in vivo* magnetic resonance spectroscopy (MRS).

The following sections give a brief overview of these gradient-based applications.

1.8.1 Crusher Gradients to Dephase Transverse Magnetization

“Crusher” gradients are used to dephase transverse magnetization and are widely used, for example, in localized *in vivo* MR spectroscopy to suppress unwanted signals arising from imperfect RF pulses. In order to calculate the required strength and duration of a gradient pulse for effective dephasing, consider the effect of a gradient, G_z , applied for a time τ as shown in Figure 1.17(a), on transverse magnetization, M_{xy} . The resonance frequency of the protons is given by eqn (1.25). If one assumes a sample with length L in the z -direction, and with uniform proton density, then the average transverse magnetization, as a function of G_z and τ , over the length L is given by:

$$M_{xy}(\tau) = \frac{1}{L} \int_{-\frac{L}{2}}^{\frac{L}{2}} M_{xy}(t=0) e^{j\gamma G_z z} dz = \frac{\sin(\gamma L G_z \tau / 2)}{\gamma L G_z \tau / 2} \tag{1.26}$$

i.e. a sinc function. Figure 1.17(b) shows a plot of the transverse magnetization as a function of time and gradient strength. If one wishes, as an example,

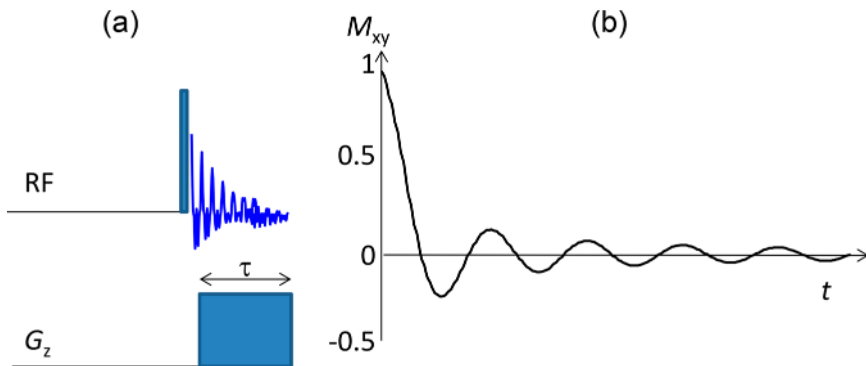


Figure 1.17 (a) Application of a gradient pulse directly after an RF pulse dephases the magnetization. (b) The time-evolution of the transverse magnetization as a function of gradient strength.

to completely dephase the magnetization for a sample of length 1 cm, then a 2 ms long gradient pulse with strength 0.37 T m^{-1} reduces the transverse magnetization by a factor of 1000.

1.8.2 Gradients for Coherence Selection in High-Resolution NMR

Many NMR experiments involve the creation and selection of multiple quantum coherences to simplify the resulting spectra. Examples include homonuclear double quantum and triple quantum coherence selection in correlated spectroscopy (COSY) experiments, as well as heteronuclear multiple quantum coherences created in triple-resonance sequences. The topic of multiple-quantum sequences is covered in many textbooks on high resolution NMR spectroscopy. Gradients can be used to select between different coherence pathways. The coherence order, p , is defined as the difference in the magnetic quantum number, m , of the relevant eigenstates, *i.e.*:

$$p = m_r - m_s \quad (1.27)$$

Longitudinal magnetization corresponds to $p = 0$, single quantum coherence transverse magnetization to $p = \pm 1$, double-quantum coherence to $p = \pm 2$, and so on. In any sequence, the coherence transfer pathway begins with $p = 0$, corresponding to thermal equilibrium magnetization along B_0 .

In order to select only the desired coherence pathway, phase cycling can be used, *i.e.* repeating the sequence a number of times with different phases of the RF pulses. This is an efficient way of coherence selection, but limits the minimum total experiment time, especially for sequences requiring extensive phase cycles (16, 32 or 64 steps). An alternative method of selecting specific coherence orders is to use gradients, using the principle that the phase accumulation of the spins during the application of the gradient pulse is proportional to the coherence order. So for a rectangular-shaped gradient pulse with strength G_z , applied for time τ , the phase ϕ is given by:

$$\phi(z, \tau) = p\gamma G_z z \tau \quad (1.28)$$

Eqn (1.28) shows, for example, that double-quantum coherences accumulate phase twice as fast as single-quantum coherence, and triple-quantum coherences three times as fast. Thus, by applying gradient pulses of different strengths or durations it is possible to refocus selective coherence orders, while unwanted coherences are dephased. Simple examples are shown in Figure 1.18 for double-quantum and triple-quantum-filtered COSY sequences.

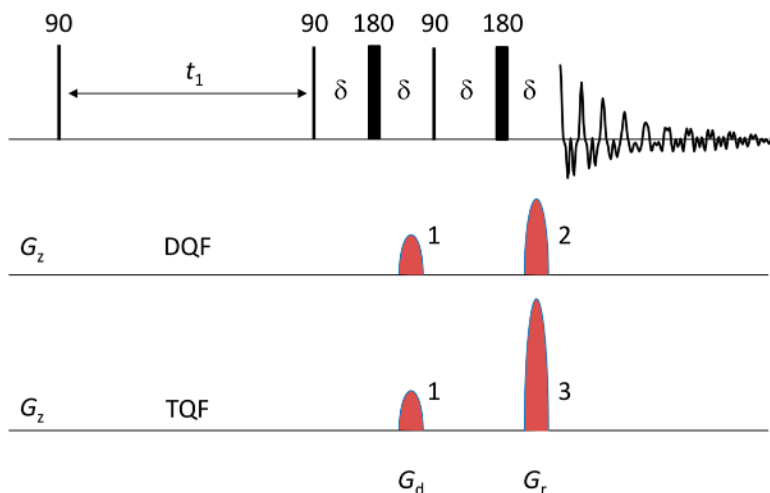


Figure 1.18 Pulse sequences for double quantum filtered (DQF) and triple quantum filtered (TQF) magnitude COSY spectra. The sequence of RF pulses is identical for both experiments. In the DQF experiment, the double quantum coherence created by the second 90° pulse is dephased by gradient G_d and the detected single quantum coherence is rephased by gradient G_r . If $G_r = 2G_d$, then DQ coherence only is refocused, if $G_r = 3G_d$ then TQ coherence only is refocused.

1.8.3 Measurements of Apparent Diffusion Coefficients Using Gradients

The phase evolution of transverse magnetization when a gradient is applied can also be used to measure the molecular diffusion coefficient of a sample. The most common sequence used for this purpose is the Stejskal-Tanner spin-echo, or variations thereof, shown in Figure 1.19.

The phase accumulation during the first gradient is given by:

$$\phi_z = \gamma \int G_z z dt = \gamma G_z z \delta \tag{1.29}$$

The 180° pulse refocuses B_0 inhomogeneities and chemical shift effects. If the diffusion coefficient of the sample is zero, then there is an equal and opposite phase accumulation produced by the gradient applied after the 180° pulse, and the effects of phase accumulation are completely rephased, the signal simply being attenuated by T_2 relaxation. However, if there is indeed a physical displacement of the molecules, *i.e.* diffusion, during the time interval between the two gradient pulses, then the two phase accumulations are not equal and the signal amplitude is attenuated. The faster the diffusion coefficient (D) the greater the signal attenuation. In the “short-pulse limit”, *i.e.* when $\delta \ll \Delta$, the signal intensity is given by:

$$S(G_z) = S(G_z = 0) e^{-\gamma^2 G_z^2 \delta^2 (\Delta - \delta/3) D} = S(G_z = 0) e^{-bD} \tag{1.30}$$

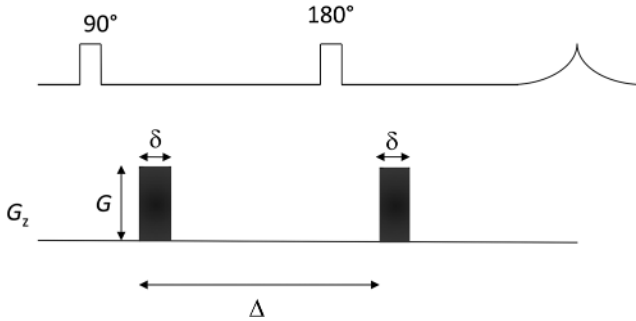


Figure 1.19 The Stejskal–Tanner spin-echo experiment used to measure the apparent diffusion coefficient (D) of a sample. The value of D can be calculated from a plot of the measured signal intensities as a function of the applied gradient strength for a series of different gradient values.

where the b -factor is defined as:

$$b = \gamma^2 G^2 \delta^2 (\Delta - \delta/3) \quad (1.31)$$

By repeating the sequence with a set of different b -values, usually *via* different values of the diffusion-encoding gradient, the resulting signal amplitudes can be fitted to eqn (1.30) to determine the value of D . In addition to measuring diffusion in homogeneous liquid samples, diffusion weighting can be used in high-resolution NMR^{21,22} to filter out signals with a very fast diffusion coefficient, for example the water signal in a protein solution. Diffusion encoding sequences are very widely used in MRI in the areas of diffusion weighted imaging (DWI),^{18,23} diffusion tensor imaging (DTI),²⁴ diffusion kurtosis imaging (DKI),^{25,26} and fiber tractography.²⁷

1.8.4 Gradient-Based Shimming

As outlined in Section 1.7, maximizing the magnetic field homogeneity for each sample involves B_0 shimming, *i.e.* optimizing the currents through each of the individual shim coils. This is a time-consuming process that is not ideal to perform manually, for example, for *in vivo* experiments. Rather than manual optimization, the process can be automated and speeded up by the use of gradients using a pulse sequence, such as the one shown in Figure 1.20(a), which measures the magnetic field inhomogeneity, $\Delta B_0(z)$ as:

$$\Delta B_0(z) = \frac{\Delta\phi(z)}{\gamma(TE_1 - TE_2)} \quad (1.32)$$

where $\Delta\phi$ is the spatially dependent phase difference between the measured projections shown in Figure 1.20(a). In terms of the shim settings, the residual magnetic field $\Delta B_{\text{res}}(z)$ can be defined as:

$$\Delta B_{\text{res}}(z) = \Delta B_0(z) - \sum_j c_j S_j(z) \quad (1.33)$$

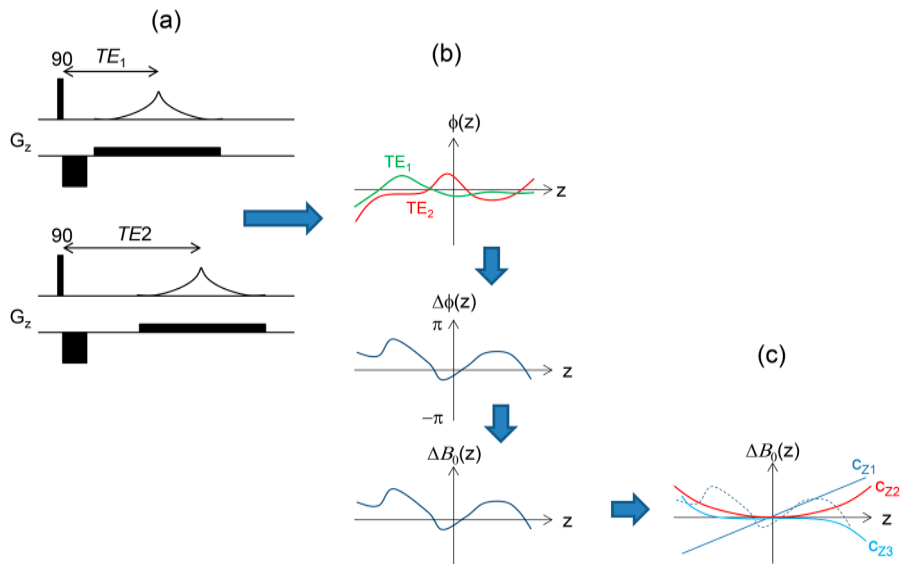


Figure 1.20 Schematic of the processes involved in gradient-based shimming. (a) One dimensional gradient projections of the sample are obtained for two different echo times, TE_1 and TE_2 . (b) The difference in the phases ($\Delta\phi$) between the two projections is calculated and scaled to give the B_0 inhomogeneity (ΔB_0) as a function of z -position. (c) Knowing the magnetic field profiles of each of the shim coils, a least-square fitting routine is implemented to calculate the currents through each of the shim coils which best compensates for the measured B_0 inhomogeneity.

where $S_j(z)$ is the magnetic field distribution of shim j , and c_j represents the corresponding weighting function. This residual is minimized by calculating the values of the coefficients c_j (*i.e.* the currents through each shim coil), which is normally performed in a least-squares sense over the entire one-dimensional z -projection:

$$\text{Min} \left[\sum_{k=1}^{N_z} |\Delta B_{\text{res}}(z_k)|^2 \right] \tag{1.34}$$

where N_z is the number of data points acquired in the z -projection.

1.8.5 Gradients in MRI

In MRI three orthogonal sets of gradients are used to spatially encode the x , y and z dimensions of the sample. Each of these gradients is designed to provide a linear variation of magnetic field as a function of spatial dimension, *i.e.*:

$$\frac{\partial B_z}{\partial z} = G_z \quad \frac{\partial B_z}{\partial x} = G_x \quad \frac{\partial B_z}{\partial y} = G_y \tag{1.35}$$

The process of image formation is covered in more detail in Section 1.11 later in this chapter. For human MRI applications, typical gradient strengths of 60–70 mT m⁻¹ are used, with some specialized gradients going up to 300 mT m⁻¹.^{28,29} High gradient values can also be produced by reduced diameter “head-only insert” gradient coils. MRI is also extensively used in pre-clinical animal imaging systems, and also for microimaging experiments on samples as small as single cells.

1.9 The Deuterium Lock Channel and Field Monitoring

Although the static magnetic field is extremely stable over time, every magnet displays small frequency “drifts” that are typically of the order of 1–10 Hz per hour. Since many NMR experiments require data acquisition times on the order of hours or even days, it is essential to compensate in real-time for this field drift. If not corrected, then spectral linewidths are broadened, and artifacts can appear in the spectrum.

In high-resolution liquid-state NMR, this correction is performed using a deuterium “lock channel”. One channel of one of the RF coils in the NMR probe is tuned to the deuterium (²H) resonance frequency. The sample is dissolved in a fully or partially deuterated solvent (e.g. D₂O, CDCl₃, or C₆D₆). Deuterium is a quadrupolar nucleus with a very short T_1 value, and so the signal can be pulsed and sampled effectively continuously. The imaginary “dispersive” component of the deuterium spectrum is monitored, as shown in Figure 1.21(a). Changes in the static magnetic field produce a shift in the dispersive spectrum, which is analyzed to define an error signal, as shown in Figure 1.21(a). This error signal forms the input to a negative feedback loop, which controls the current applied to the Z_0 shim coil. This coil is a long solenoid, which produces a uniform magnetic field which can add or subtract from the main B_0 field. Since the deuterium signal can be quite noisy (owing to the low power used for pulse transmission, the low gamma of the deuterium nucleus, and the low sensitivity of the deuterium channel of the RF coil), the deuterium signal is averaged over many hundreds or thousands of samples so that the current in the Z_0 shim is only updated slowly. The negative feedback loop is designed such that it integrates the deuterium signals over a long period of time, and thus has a very slow time-constant. The lock channel effectively forms a separate simple “spectrometer”, linked by a central clock/master oscillator to the rest of the data acquisition system.

The lock-channel can also be used to monitor the static field homogeneity during shimming. The better the homogeneity the sharper the deuterium line shape and the higher its amplitude. This system is still present on many high-resolution NMR systems but gradient-based shimming, as described in Section 1.8.4, is increasingly being used.

For most *in vivo* MRI and MRS experiments there are not as stringent requirements for the stability of the magnetic field as there are in high-resolution

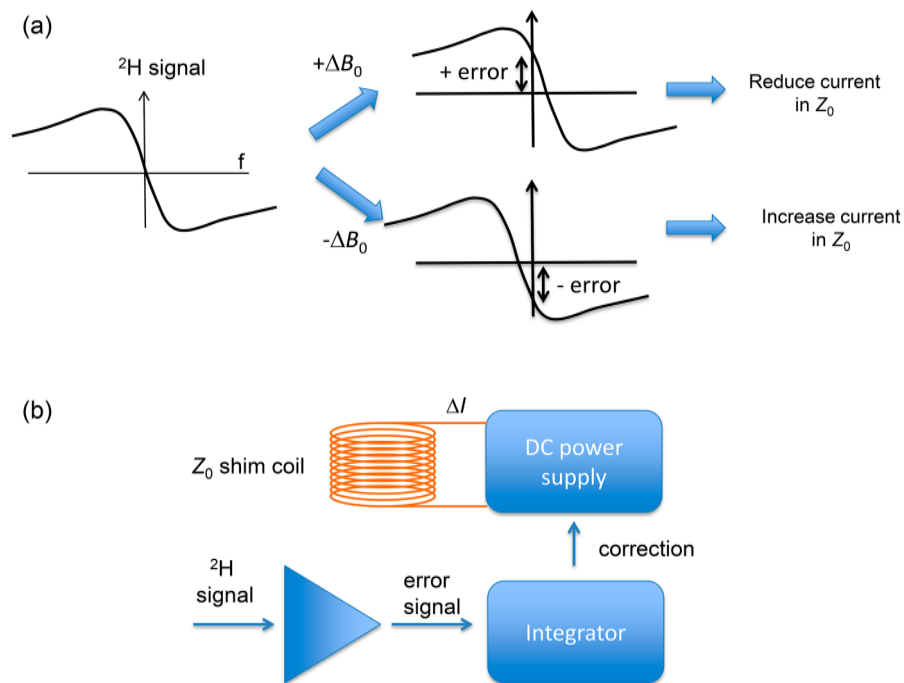


Figure 1.21 Schematic of the operation of the deuterium-based frequency lock on a high-resolution NMR system. (a) A drift in the magnetic field shifts the deuterium resonance to a higher or lower frequency. The dispersive line shape is monitored and a corresponding positive or negative “error” signal recorded as the signal intensity at zero frequency in the rotating reference frame. (b) This error signal is integrated over time and, *via* a negative feedback loop, alters the current (ΔI) fed into the Z_0 shim coil to correct for the magnetic field drift.

NMR. Experiments typically do not take as long, spectral linewidths *in vivo* are much wider owing to the intrinsic inhomogeneity of biological tissue, and imaging *per se* is much more robust with respect to small frequency drifts than spectroscopy. Therefore, in MRI systems there is no need for a separate lock channel. However, in MRI there are other mechanisms that can lead to drifts in the magnetic field. In sequences requiring rapid switching of the gradients, significant temperature changes can occur in the gradient coil, which in turn can heat components such as the passive iron shims and field booster rings. These thermal disturbances change the magnetic susceptibility of the component iron, and hence cause a change in the magnetic field. Changes owing to gradient heating are relatively slow owing to the large heat capacity of the physical former on which the gradient coils are wound, and the large mass of the structure, and so monitoring does not have to be continuous but can be interspersed between scans using very low tip angle spectroscopic measurements of the water resonance frequency, since it is the dominant species for *in vivo* measurements. Based on these measurements,



Figure 1.22 A photograph of a commercial field-monitoring system using a series of microcoils (encased in black plastic), tuned to the fluorine resonance, with a fluorinated sample inside. By continuous measurement of the phase of the fluorine MR signal, spatial and temporal variations in the magnetic field can be measured and corrected either in real-time or in signal post-processing.

rather than changing the magnetic field itself as described for the deuterium lock, the system simply alters the frequencies of the transmitter and receiver.

Although this type of monitoring can be used to compensate for global changes in the magnetic field, it cannot correct for spatially dependent changes, which, in addition to gradient heating, can be caused by many other factors, such as patient motion. Correcting for spatially dependent changes in the magnetic field clearly requires spatially dependent measurements. These can be implemented, for example, using multiple small microcoil probes that contain a fluorinated liquid and, similarly to the deuterium lock channel on a high-resolution NMR system, form a separate but linked MR spectrometer.³⁰ The use of multiple fluorinated probes, shown in Figure 1.22, allows the extraction of spatial variations in the main magnetic field, and the ability to apply real-time corrections to compensate for these fluctuations.

1.10 Magic Angle Spinning Solid-State NMR: Principles and Instrumental Requirements

NMR spectra of liquid samples consist of a series of very sharp resonances, owing to the averaging of anisotropic NMR interactions by rapid random tumbling, resulting in very long T_2 values, typically hundreds of milliseconds. In contrast, NMR spectra of solid or rigid samples are very broad, since anisotropic and orientation-dependent interactions are not averaged: an example is shown in Figure 1.23(a). The two most important interactions

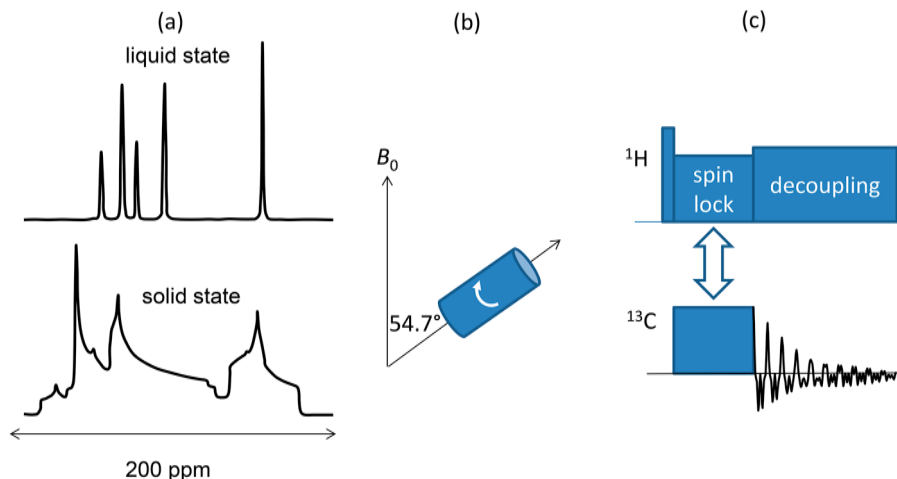


Figure 1.23 (a) Schematics of the respective spectra for ^{13}C in the liquid and solid states. (b) Spinning the sample at the magic angle (54.7°) with respect to B_0 is used to reduce the effect of dipolar coupling and chemical shift anisotropy. (c) A pulse sequence used for heteronuclear solid-state spectroscopy involving cross-polarization and high-power proton decoupling.

that produce broad linewidths in solids are dipolar coupling and chemical shielding, with the dipolar term being dominant especially at low magnetic fields.

Dipolar coupling results from the interaction of one nuclear spin with the magnetic field generated by a second nuclear spin, and *vice versa*. Dipolar coupling represents a direct through-space interaction, the magnitude of which is given by:

$$R_{jk}^{\text{DD}} = \frac{\mu_0 \hbar \gamma_j \gamma_k}{4\pi \langle r_{jk} \rangle^3} \quad (1.36)$$

where R_{jk}^{DD} is the dipolar coupling between two spins j and k , and r_{jk} is the distance between the spins.

Chemical shielding is related to the chemical shift outlined earlier for liquid samples, and is an anisotropic interaction characterized by a shielding tensor. Anisotropy in the chemical shift leads to broadening of the spectral lines. For molecules which are spatially symmetric in three-dimensions the chemical shift anisotropy (CSA) is very small. For non-symmetric molecules, the CSA is larger, and linewidths correspondingly wider.

Both dipolar coupling and chemical shielding have an angular dependence with respect to B_0 , containing multiplicative terms $(3 \cos^2 \theta - 1)$, where θ is the angle between a line connecting the two nuclei and B_0 for the dipolar coupling, and between the direction with the largest deshielding

and B_0 for the chemical shift term. One can therefore effectively average out these components by rotating the sample very rapidly at an angle of 54.74° with respect to B_0 such that $3 \cos^2 \theta - 1 = 0$, a technique termed magic-angle spinning (MAS),³¹ illustrated in Figure 1.23(b). For full averaging the rate of spinning must be greater than the anisotropic interaction. State-of-the-art microprobes are able to spin at a rate of 111 kHz.³² For regular-sized samples, typical diameter/spinning speeds are 1.3 mm diameter/65 kHz, 2.5 mm/35 kHz, 3.2 mm/23 kHz, 4 mm/8 kHz, and 7 mm/4 kHz. Since proton dipole–dipole coupling constants can be much greater than 100 kHz, full averaging is rarely achieved and MAS is often combined with multiple-pulse sequences, which also reduce the effects of dipolar coupling, based on concepts originally developed as WAHUA³³ or MREV-8.^{34,35} The combination of MAS with multiple-pulse sequences is called CRAMPS (Combined Rotation and Multiple-Pulse Sequence) and requires high-power amplifiers, short RF times, and fast switching between the transmit and receive mode.

For dilute spin-1/2 nuclei, such as ^{13}C , the homonuclear (^{13}C – ^{13}C) dipolar coupling is insignificant owing to its low occurrence. The ^1H – ^{13}C heteronuclear dipolar coupling can be minimized with high-power proton decoupling,^{33,36} as shown in Figure 1.23(c). The sensitivity of this type of experiment can be increased using cross-polarization (CP)³⁷ techniques, which involve polarization transfer from ^1H to ^{13}C . Efficient CP requires that the precessional frequencies in the rotating frame are the same for protons and carbon, *i.e.*:

$$\gamma_{\text{C}} B_{1,\text{C}}^+ = \gamma_{\text{H}} B_{1,\text{H}}^+ \quad (1.37)$$

This requirement implies that the B_1^+ fields must be spatially homogeneous at both frequencies, and as discussed in Chapter 3 this requires that the coils be very well balanced, which is challenging, particularly at very high frequencies. Cross-polarization is generally combined with relatively low-speed MAS (5 to 15 kHz) in a combined approach known as CP–MAS.

In a similar fashion to that described previously for liquid-state NMR, gradient coils can be incorporated into the probe in order to perform coherence pathway selection in multiple quantum solid-state experiments. In this case, the gradients must be oriented along the magic angle.^{38,39}

The instrumental requirements corresponding to the types of experiments outlined above include:

- (i) The ability to spin the sample extremely rapidly with a high degree of mechanical precision.
- (ii) Very short ($\sim 1 \mu\text{s}$), high-power RF pulses must be applied, which place high degrees of demand on the RF amplifiers and components in the RF probe.
- (iii) The RF fields for different nuclei must be spatially very well matched and homogeneous for efficient cross-polarization.

- (iv) Isolation between the receive chains of the different nuclei, as well as between transmit and receive chains, must be very high since high-power decoupling may be applied during data acquisition.
- (v) Magic angle gradients and associated gradient amplifiers must be capable of producing gradient pulses with durations below 100 μs and strengths of 500 mT m^{-1} .

1.11 Magnetic Resonance Imaging: Principles and Instrumental Requirements

In MRI there are a large number of different imaging sequences, which can be used for structural imaging, functional imaging, magnetic resonance angiography, and diffusion-weighted imaging, to name only a few.¹² Two generic sequences, or “building-blocks”, are shown in Figure 1.24, namely a gradient-echo and spin-echo sequence.

In the sequences shown in Figure 1.24 there are three “processes” used to produce the two-dimensional image. First, slice-selection uses a frequency-selective RF pulse applied simultaneously with a magnetic field gradient, denoted by G_{slice} . If the selective RF pulse, with an excitation bandwidth of $\pm\Delta\omega_s$, is applied at a frequency ω_s , then protons precessing at frequencies between $\omega_s + \Delta\omega_s$ and $\omega_s - \Delta\omega_s$ are rotated from the z-axis into the transverse plane, whereas protons with precession frequencies outside this range do not experience the RF pulse, as shown in Figure 1.25(a). By changing the centre frequency (ω_s) of the RF pulse, the slice can be centred at different parts of the sample. As indicated in Figure 1.25(b), the thickness of the slice can be decreased by using a larger gradient strength or a longer duration RF pulse that has a smaller frequency bandwidth.

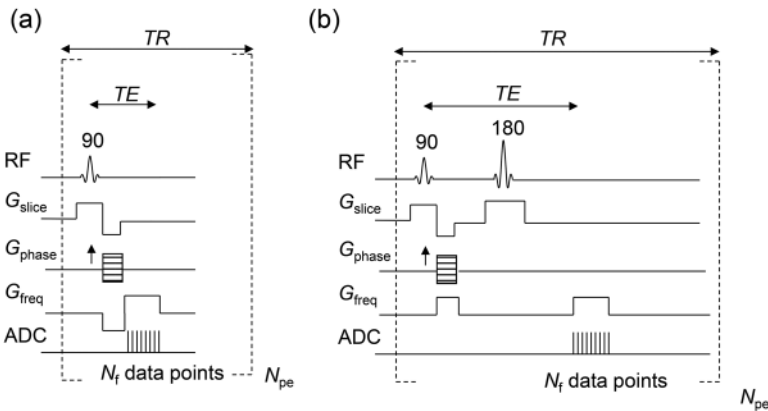


Figure 1.24 (a) Generic two-dimensional gradient-echo imaging sequence. The sequence is repeated N_{pe} times, with the phase encoding gradient being incremented from its maximum negative value to its maximum positive value. (b) Corresponding generic spin-echo imaging sequence. TR represents the repetition time and TE the echo time.

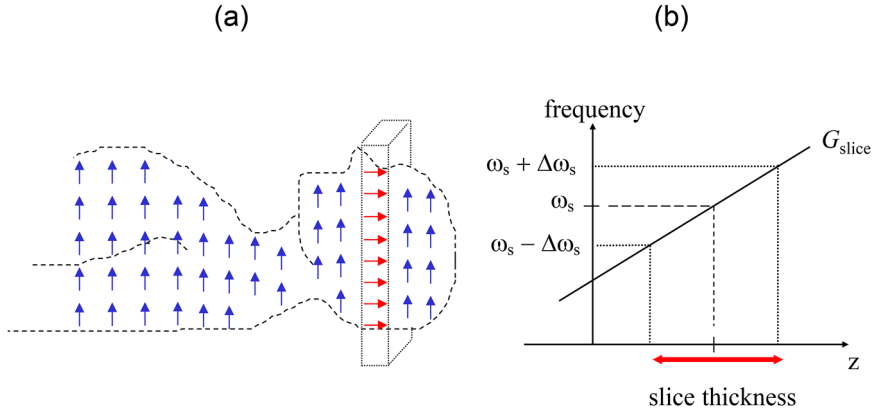


Figure 1.25 The principle of slice selection in MRI. (a) By applying a frequency-selective RF pulse in combination with a gradient, only the nuclei within a thin “slice” experience the RF pulse and are rotated from the longitudinal axis (blue) into the transverse plane (red). (b) The thickness of the slice can be controlled by the strength of the gradient and the bandwidth of the RF pulse.

Having selected a slice, a phase encoding gradient is applied to encode an orthogonal direction *via* the phase of the signal. After the phase encoding gradient has been switched off, the frequency-encoding gradient (G_{freq}) is turned on and data acquisition begins. N_f data points are sampled while the frequency encoding gradient is on, after which a relaxation delay (TR) occurs before the sequence is repeated using the next incremented value of the phase-encoding gradient. A total of N_{pe} phase encoding gradients are used, resulting in a total imaging time of $\text{TR} \times N_{\text{pe}}$.

Assigning the G_y gradient to phase encoding, and G_x to frequency encoding, the combined effect of the phase-encoding and frequency-encoding gradients gives a signal:

$$s(G_y, \tau_{\text{pe}}, G_x, t) \propto \int_{\text{slice}} \int_{\text{slice}} \rho(x, y) e^{-j\gamma G_x x t} e^{-j\gamma G_y y \tau_{\text{pe}}} dx dy \quad (1.38)$$

where τ_{pe} is the time for which the phase encoding gradient is applied. Two variables k_x and k_y can be defined as:^{40,41}

$$k_x = \frac{\gamma}{2\pi} G_x t \quad k_y = \frac{\gamma}{2\pi} G_y \tau_{\text{pe}} \quad (1.39)$$

and eqn (1.38) can be re-expressed as:

$$S(k_x, k_y) \propto \int_{\text{slice}} \int_{\text{slice}} \rho(x, y) e^{-2\pi j k_x x} e^{-2\pi j k_y y} dx dy \quad (1.40)$$

The $N_f \times N_{\text{pe}}$ data matrix can be visualized as a two-dimensional dataset as a function of k_x and k_y , commonly referred to as the k -space domain. Consider

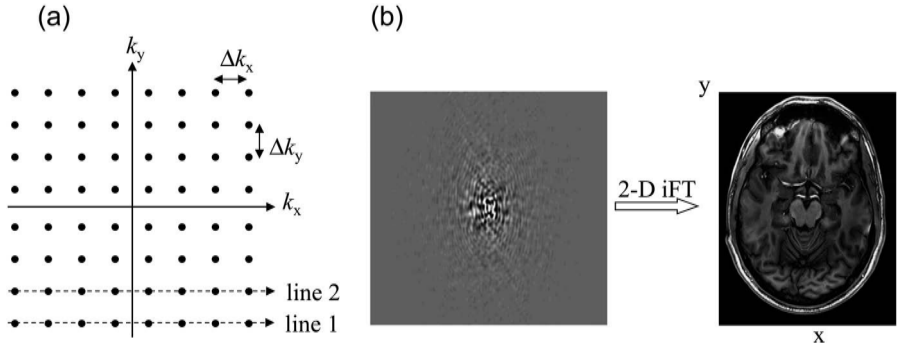


Figure 1.26 (a) Data for MRI are acquired in “ k -space”, with a Cartesian grid shown in this case. (b) The image is reconstructed by a two-dimensional inverse Fourier transform of the k -space data.

the N_f data points collected when the maximum negative value of the phase-encoding gradient, G_y , is applied. From eqn (1.39) the value of k_y for all N_f data points corresponds to its maximum negative value. When the frequency-encoding gradient is switched on, the first data point collected corresponds to the maximum negative value of k_x due to the negative dephasing lobe shown in Figure 1.24(a), the second data point to a slightly more positive value of k_x and so forth, and so the N_f data points correspond to one “line” in k -space, shown as line 1 in Figure 1.26(a). The second line in k -space corresponds to the next value of the phase-encoding gradient, and so on. The spacing between the k -space points is inversely proportional to the respective spatial dimensions, or fields-of-view (FOV), in the image: $\Delta k_x = 1/\text{FOV}_x$, $\Delta k_y = 1/\text{FOV}_y$.

A two-dimensional inverse Fourier transform of the k -space data $S(k_x, k_y)$ gives $\rho(x,y)$, which is the MR image, as shown in Figure 1.26(b). MR images are conventionally represented as the magnitude of $\rho(x,y)$.

$$\rho(x,y) \propto \int_{-\infty}^{\infty} \int_{-\infty}^{\infty} S(k_x, k_y) e^{+j2\pi(k_x x + k_y y)} dk_x dk_y \tag{1.41}$$

The signal intensity in each voxel of the image depends on the tissue relaxation times as well as the proton density. In terms of the MR relaxation times, for an axial image acquired using slice-selection in the z -direction, the image intensity of each voxel, $I(x,y)$, is given by:

$$I(x,y) \propto \rho(x,y) \frac{\left(1 - e^{-\frac{\text{TR}}{T_1}}\right) \sin \alpha}{1 - e^{-\frac{\text{TR}}{T_1}} \cos \alpha} e^{-\frac{\text{TE}}{T_2}} \tag{1.42}$$

where $\rho(x,y)$ is the “proton density” and the tip angle of the RF pulse in the gradient echo sequence is α . The degree of T_1 -weighting of the image

is determined by the respective values of the tissue T_1 and the chosen TR interval between repeated phase-encoding steps: if $TR \ll T_1$ then there is no weighting, whereas if $TR \approx T_1$ then the image intensity is weighted by different tissue T_1 relaxation times. Similarly, the situation of $TE \approx T_2^*$ introduces T_2^* -weighting into the image.

Although eqn (1.42) indicates that the SNR is maximized using a value of $\alpha = 90^\circ$, this case would require a long value of TR to allow full T_1 relaxation to occur, and as a result an impractically long data acquisition time for clinical applications. In order to image more rapidly, the value of α is reduced to a value considerably smaller than 90° . For a given value of TR, the value of α that maximizes the signal intensity is given by:

$$\alpha_{\text{Ernst}} = \cos^{-1} e^{-\frac{TR}{T_1}} \quad (1.43)$$

For example, if TR is reduced to $0.05 T_1$, then the optimum value of α is 8° . Using these parameters, images can be acquired in a few tens of seconds.

Gradient-echo sequences allow very rapid image acquisition. The major disadvantage is that they are weighted by tissue T_2^* values, which are typically much shorter than T_2 *in vivo*. In order to introduce pure T_2 -contrast into the image a spin-echo sequence can be used, as shown in Figure 1.24(b). The spatial encoding principles are exactly the same as for the gradient echo image, but now the intensity is weighed by the T_2 rather than T_2^* value:

$$I(x, y) \propto \rho(x, y) \left(1 - e^{-\frac{TR}{T_1}} \right) e^{-\frac{TE}{T_2}} \quad (1.44)$$

As mentioned previously there are very many types of MRI sequences. Common instrumental requirements include:

1. RF coils and RF amplifiers must be able to handle/provide up to 30–60 kW of power, with duty cycles up to ~20%. The pulses are both amplitude and phase modulated, with strict requirements for the reproducibility. The amplifiers must be linear over a large range of signal inputs/outputs.
2. For rapid imaging sequences such as echo planar imaging, gradient switching rates in the hundreds of hertz to kilohertz may be necessary. In this case, one also needs to consider peripheral nerve stimulation (PNS), which can occur when the dB/dt is on the order of 50–100 T s⁻¹.
3. Data acquisition involves much higher bandwidths than for spectroscopic experiments: fast imaging sequences may have bandwidths up to 1 MHz for very high gradient strengths.
4. The amount of streaming data is very high: a commercial 32-channel receive array may acquire data essentially continuously over 20 minutes, representing several gigabytes of data that has to be processed in real-time for clinical evaluation.

Appendices

As seen in this first chapter, the hardware components of the MR system share many geometric properties and design goals. A cylindrical geometry is inherent in superconducting magnet design, RF volume coils, shim coils and gradient coils. Maximizing the homogeneity of the magnetic field is critical for superconducting magnet and RF coil design; producing a linear spatial variation in magnetic field is key for gradient coil design; and well-defined higher-order spatial distributions of the magnetic field are required for shim coil design. The basis for each of these component is a set of current-carrying electrical conductors. Despite the fact that the operating frequencies of these different components are quite different (DC for magnets and shim coils, tens to hundreds of kHz for gradients, and tens to hundreds of MHz for RF coils), there are common mathematical tools that can be used to produce the desired magnetic field distributions. Two of the most common formalisms, namely the Biot–Savart law and spherical harmonic decomposition, together with specific examples of their use, are described in these two appendices. These models are further refined, and more sophisticated examples given, in several of the chapters later in the book.

Appendix A. Maxwell's Equations and the Biot–Savart Law

The fundamental bases for calculating both magnetic and electric fields are termed Maxwell's equations, listed in eqn (1.45–1.48).

$$\nabla \cdot E = \frac{\rho_v}{\epsilon} \text{(Gauss' law)} \quad (1.45)$$

$$\nabla \cdot H = 0 \text{(Gauss' law for magnetism)} \quad (1.46)$$

$$\nabla \times E = -\mu \frac{\partial H}{\partial t} \text{(Faraday's law)} \quad (1.47)$$

$$\nabla \times H = J + \epsilon \frac{\partial E}{\partial t} \text{(Ampere's law)} \quad (1.48)$$

where ρ_v is the electric charge density, ϵ the permittivity, μ the permeability, H the magnetic field, E the electric field, and J the electric current density. The operators on the left of eqn (1.45) and (1.46) represent divergence, and those in eqn (1.47) and (1.48) represent curl operators. In physical terms, the divergence of a vector field describes the degree to which it behaves as either a source or a sink at a given point. If the divergence is non-zero at some point then there must be a source or sink at that position: in contrast, if the divergence is zero then it indicates that there is neither. The curl operators on the left of eqn (1.47) and (1.48) represent the spatial-variation of the electric and

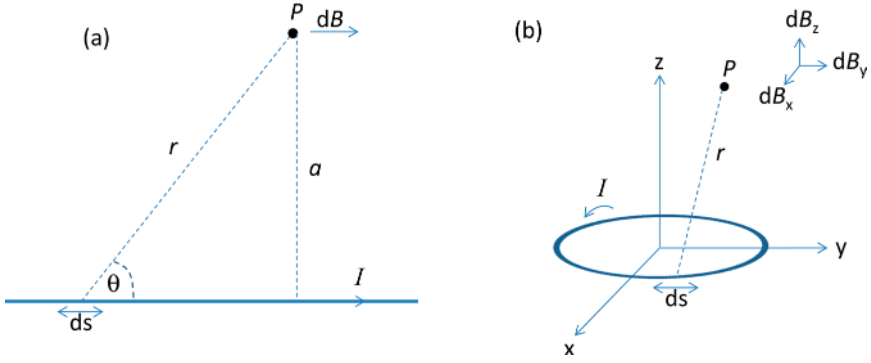


Figure 1.27 Examples of (a) a current-carrying straight wire and (b) a current-carrying circular wire-loop, for calculation of magnetic fields using the Biot-Savart law.

magnetic fields, which are coupled to the time-variation of the magnetic and electric fields on the right hand side. In other words, as an electric field propagates throughout the sample it gives rise to a time-varying magnetic field. This magnetic field, which varies as a function of space, in turn gives rise to a time-varying electric field. Eqn (1.47) and (1.48) show that magnetic and electric fields are intrinsically coupled.

Designs for magnets, gradient coils, shim coils or RF coils can be formulated by simplifying Maxwell’s equations under conditions known as “quasi-static”, which corresponds to being able to neglect any effects of the finite wavelength of the EM wave within the sample. In this case, the magnetic field can be estimated quite accurately by the Biot-Savart law, which can be derived directly from Maxwell’s equations. The Biot-Savart law describes the magnetic field (dB) at a point P distance r from the wire, produced by a current I flowing through a small section (ds) of wire. The value of dB is given by:

$$d\vec{B} = \frac{\mu_0}{4\pi} I \frac{d\vec{s} \times \vec{r}}{r^3} \tag{1.49}$$

where μ_0 is the permeability of free space, equal to $1.257 \times 10^{-6} \text{ T m A}^{-1}$. Two very simple examples are given below, a straight wire and a circular loop, both shown in Figure 1.27.

Example A1. Magnetic Field Produced by a Straight Wire

In Figure 1.27(a), the value of dB for a straight wire can be calculated by simple trigonometry:

$$d\vec{B} = \frac{\mu_0}{4\pi} I \left(\frac{\sin \theta}{a} \right)^2 \sin \theta dx \tag{1.50}$$

The total magnetic field produced by the current in the infinitely long wire is then simply given by the integral of this expression:

$$B = \frac{\mu_0 I}{4\pi a} \int_0^\pi -\sin \theta d\theta = \frac{\mu_0 I}{2\pi a} \tag{1.51}$$

The result shows that the magnetic field decreases as the inverse of distance from the wire.

Example A2. Magnetic Field Produced by a Circular Wire Loop

Consider a loop of wire with radius a , shown in Figure 1.27(b). If one considers the field produced along the central axis of the loop, there is only one non-zero component of the magnetic field, which is oriented along the z -direction and is given by:

$$B_z = \frac{\mu_0 a^2 I}{2(z^2 + a^2)^{3/2}} \tag{1.52}$$

So at the centre of the loop, the magnetic field is given by $\mu_0 I/2a$, *i.e.* the smaller the wire loop the higher the magnetic field produced per unit current. Along the central axis of the coil, *i.e.* along the z -axis, the magnetic field decreases approximately exponentially with distance.

The off-axis magnetic fields can also be calculated analytically, but are more complicated. They are given (in polar coordinates) by:

$$\begin{aligned} B_r &= \frac{\mu_0 I}{2\pi} \frac{z}{r \left[(a+r)^2 + z^2 \right]^{1/2}} \left[\frac{a^2 + r^2 + z^2}{(a-r)^2 + z^2} E(k) - K(k) \right] \\ B_\theta &= 0 \\ B_z &= \frac{\mu_0 I}{2\pi} \frac{z}{r \left[(a+r)^2 + z^2 \right]^{1/2}} \left[\frac{a^2 - r^2 - z^2}{(a-r)^2 + z^2} E(k) + K(k) \right] \end{aligned} \tag{1.53}$$

where E and K are complete elliptical integrals of the second and first kinds, respectively, and k is defined as:

$$k = \sqrt{\frac{4ar}{(a+r)^2 + z^2}} \tag{1.54}$$

Using these analytical results, designs using circular loops in particular can be optimized in terms of producing the desired spatial distribution of the

magnetic field. The following two examples show the application in designing a linear magnetic field gradient and a homogeneous magnetic field, both with a simple two-loop arrangement.

Example A3. Design of a Two-Loop Coil Geometry to Produce a Linear z-Gradient

The simplest configuration for a coil producing a gradient in the z-direction is a “Maxwell pair”, shown in Figure 1.28(a), which consists of two separate loops of multiple turns of wire, each loop containing equal currents, I , flowing in opposite directions. In order to estimate the distance between the two loops that maximizes the linearity of the gradient, the value of B_z is first calculated using eqn (1.52):

$$B_z = \frac{\mu_0 I a^2}{2[(d/2 - z)^2 + a^2]^{1.5}} - \frac{\mu_0 I a^2}{2[(d/2 + z)^2 + a^2]^{1.5}} \tag{1.55}$$

where μ_0 is the permeability of free space and a is the radius of the gradient set. By applying a Taylor series expansion, and noting that by symmetry the first two differentiable terms are zero, the first term that can give a non-linear contribution is the third derivative, given by:

$$\frac{d^3 B_z}{dz^3} = \frac{15\mu_0 I a^2}{2} \left\{ \frac{4(d/2 - z)^3 - 3(d/2 - z)a^2}{[(d/2 - z)^2 + a^2]^{9/2}} + \frac{4(d/2 + z)^3 - 3(d/2 + z)a^2}{[(d/2 + z)^2 + a^2]^{9/2}} \right\} \tag{1.56}$$

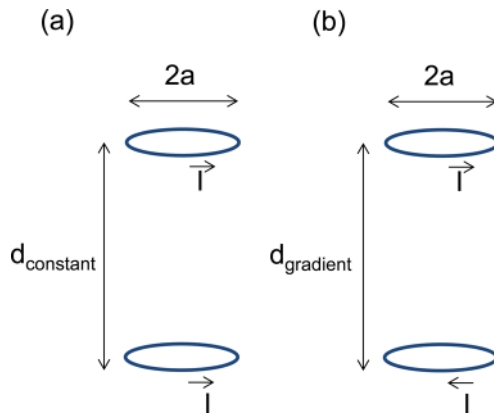


Figure 1.28 Physical arrangements of wire loops for (a) a linear gradient and (b) a constant homogeneous field. The values of d_{gradient} and d_{constant} are derived in terms of the coil radius a in examples A3 and A4.

This term becomes zero at a value of $d = a\sqrt{3}$. The magnetic field produced by this gradient coil is zero at the centre of the coil, and is linearly dependent upon position in the z -direction over about one-third of the separation of the two loops. The region over which the gradient is linear can be extended by adding other sets of coils in the axial dimension, as covered later in more detail in Chapters 2 and 4.

Example A4. Design of a Two-Loop Coil Geometry to Produce a Homogeneous Magnetic Field

Using the same arrangement as before, except with the currents now flowing in the same direction shown in Figure 1.28(b), the first-order term in the Taylor expansion is zero, and so the first perturbation arises from the second order term, which should therefore be set to zero, *i.e.*:

$$\frac{\partial^2 B_z}{\partial z^2} = 0 \quad (1.57)$$

Combining eqn (1.55) and (1.57) gives the optimum value of the distance between the coils equal to the radius of each coil. In this case the magnetic field at the centre of the coil is given by:

$$B_{z=0} = \left(\frac{4}{5}\right)^{3/2} \frac{\mu_0 n I}{a} \quad (1.58)$$

Appendix B. Spherical Harmonic Representation of Magnetic Fields

As seen in Appendix A, the Biot–Savart law is an effective method for optimizing the design of simple geometries in terms of their behaviour on-axis. However, it becomes much more cumbersome to use when one needs to consider off-axis terms. In this case, a very widely used formalism is to represent magnetic fields in terms of spherical harmonics, as described in a simplified form below.

Visual Description

The starting point is to consider the magnetic field within a sphere of a certain diameter positioned at the centre of the magnet. If the aim is to produce a homogeneous magnetic field then one can clearly define the desired field by a single vector term B_z with fixed amplitude and direction within the sphere. As will be seen in Chapter 2, this is not possible to achieve in practice (theoretically one can achieve this only by passing current through an infinitely long solenoid) and there will be spatial perturbations in the magnetic field. As in many other areas of engineering one can define these

perturbations in terms of increasing orders, *i.e.* first-order, second-order *etc.* In the case of spherical harmonics, there are three first order perturbations, five second order, seven third order, and so on. Within each order, there are a number of degrees, *e.g.* five degrees within the second order, seven degrees within the third order *etc.* The order is given the symbol n , and the degree the symbol m . The zero order term ($m = 0, n = 0$) represents a homogeneous magnetic field. The three first order ($n = 1$) perturbations correspond to linear variations in magnetic field, with the three orthogonal directions obviously being x, y and z . The degree (m) of the perturbation corresponds to the particular direction, with $m = +1$ being $x, m = 0$ being z , and $m = -1$ being y . The five second order terms ($n = 2$) correspond to $m = +2, +1, 0, -1$ and -2 . Figure 1.29 shows the spatial distributions of the zero, first and second order spherical harmonics.

If one considers only the terms with $m = 0$, one can see that these are rotationally invariant with respect to the z -axis: these are called zonal harmonics. Considering the spheres to have longitudinal and latitudinal axes, analogous to a globe, there are $2|m|$ zeroes in the longitudinal axis and $n - |m|$ zeroes in the latitudinal one.

Mathematical Description of Spherical Harmonics

Starting from Gauss' law of magnetism and Ampere's law, eqn (1.47) and (1.48), one can derive a very useful equation, which is referred to as Laplace's equation.

$$\nabla^2 B_x = \nabla^2 B_y = \nabla^2 B_z = 0 \tag{1.59}$$

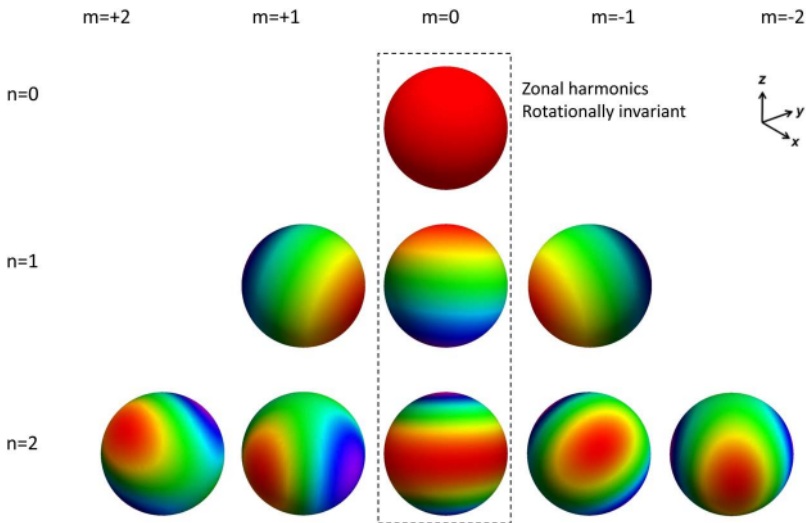


Figure 1.29 Visual representation of lower order spherical harmonics.

where the differential Laplacian operator is defined as:

$$\nabla^2 = \frac{\partial^2}{\partial x^2} + \frac{\partial^2}{\partial y^2} + \frac{\partial^2}{\partial z^2} \tag{1.60}$$

In the case of an MR magnet, the magnetic field is aligned along one axis (the z-axis), and so one can simplify the equation to give:

$$\nabla^2 B_z = 0 \tag{1.61}$$

This equation is often solved in cylindrical coordinates (the derivation is long and complicated and covered in many textbooks so is not repeated here), shown in Figure 1.30, where θ and ϕ are the polar and azimuthal angles, respectively, and r is the radius.

The solution to Laplace's equation results in a magnetic field $B(r, \theta, \phi)$ which can be described by an expansion of orthogonal spherical harmonic functions Y_{nm} and coefficients $C_{n,m}$.

$$B(r, \theta, \phi) = \sum_{n=0}^{\infty} \sum_{m=-n}^{+n} C_{n,m} r^n Y_{nm}(\theta, \phi) \tag{1.62}$$

where n is the order and m the degree, as outlined in the previous section. Spherical harmonic functions are defined on the surface of a sphere, and are given by:

$$Y_{n,m}(\theta, \phi) = C_{n,m} r^n P_{n,m}(\cos \theta) \cos(m\phi - \phi_{n,m}) \tag{1.63}$$

where $C_{n,m}$ and $\phi_{n,m}$ are constants ($\phi_{n,m} = 0$ for $m \geq 0$ and $\pi/2$ for $m < 0$), and $P_{nm}(\cos \theta)$ are polynomial functions known as Legendre polynomial functions

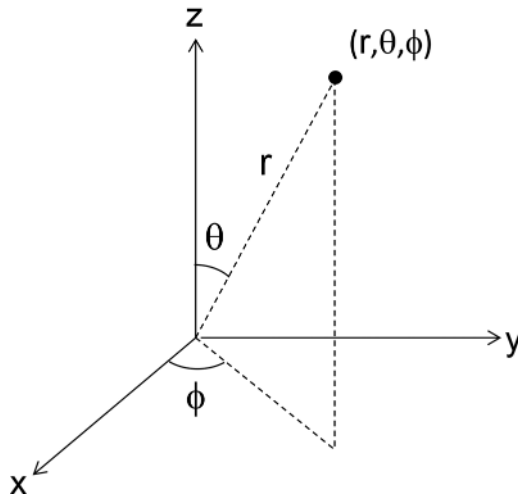


Figure 1.30 Cylindrical axis used for the description of spherical harmonic functions.

for $m = 0$, and associated Legendre polynomial functions for $m \neq 0$. Legendre polynomial functions can be calculated from:

$$P_n(x) = \frac{1}{2^n n!} \frac{d^n}{dx^n} [(x^2 - 1)^n] \tag{1.64}$$

and associated Legendre polynomials *via*:

$$P_n^m(x) = (-1)^m (1 - x^2)^{m/2} \frac{d^m}{dx^m} [P_n(x)] \tag{1.65}$$

Combining eqn (1.62) and (1.63), the magnetic field can be expressed as:

$$B(r, \theta, \phi) = \sum_{n=0}^{\infty} \sum_{m=-n}^{+n} C_{n,m} r^n P_{n,m}(\cos \theta) \cos(m\phi - \phi_{m,n}) \tag{1.66}$$

Table 1.2 gives the mathematical values of the lower order spherical harmonics that correspond to those shown in Figure 1.29.

To relate this mathematical description to the visual one presented earlier, one can consider a number of simple cases:

- (i) All cases with $m = 0$. From eqn (1.66) the magnetic field is independent of ϕ , *i.e.* it is rotationally invariant around the z -axis. For the particular case that $n = 0, m = 0$, the magnetic field is constant. When $m = 0$, the remaining Legendre polynomials are referred to as *zonal* harmonics, and give rise to what is termed a *zonal* magnetic field.

$$B_{z,zonal} = C_n r^n P_n(\cos \theta) \tag{1.67}$$

If $\theta = 0$, *i.e.* along the z -axis:

$$B_z = C_n z^n P_n(1) = C_n z^n \tag{1.68}$$

Since $P_n(1) = 1$, this can be expanded to give:

$$B_z = C_0 + C_1 z + C_2 z^2 + C_3 z^3 \dots \tag{1.69}$$

Table 1.2 Legendre and associated Legendre functions $P_{n,m}(\cos \theta)$.

		$P_{0,0}(\cos \theta)$		
		1		
	$P_{1,1}(\cos \theta)$	$P_{1,0}(\cos \theta)$	$P_{1,-1}(\cos \theta)$	
	$\sin \theta$	$\cos \theta$	$\sin \theta$	
$P_{2,2}(\cos \theta)$	$P_{2,1}(\cos \theta)$	$P_{2,0}(\cos \theta)$	$P_{2,-1}(\cos \theta)$	$P_{2,-2}(\cos \theta)$
$3 \sin^2 \theta$	$3 \sin \theta \cos \theta$	$1/2(3 \cos^2 \theta - 1)$	$3 \sin \theta \cos \theta$	$3 \sin^2 \theta$

This expression is very useful in determining parameters in, for example, gradient coil design as covered in the examples at the end of this Appendix.

- (ii) When $m \neq 0$, the magnetic field around the z axis “oscillates” with a frequency $m\phi$ and initial phase $\phi_{n,m}$. For the case that $m = +1$, the field around the circumference should exhibit one cycle, and for $m = -1$ also for one cycle but with a $\pi/2$ phase shift in the origin of the cycle. Similarly for $m = +2$ and -2 , there are two cycles circumferentially, as seen in Figure 1.29. Spherical harmonics with $m \neq 0$ are referred to as *tesseral* harmonics.
- (iii) For $n = \pm 1$ and $m = 0$ the function is rotationally invariant, and there is one cycle as a function of θ .
- (iv) For $n = 1, m = \pm 1$ the number of zeros as a function of θ is zero. These correspond to what are termed as *sectoral* harmonics, corresponding to the case $n = |m|$. Since $|m| = 1$ then there is one cycle around the circumference.

Having given a mathematical description of spherical harmonics, the final step is to show how these can be used in very simple examples of generating specific spatial distributions of the magnetic field. The first two cases are identical to those solved in Appendix A to show the correspondence between the two techniques.

Example B1. Generation of a Homogeneous Magnetic Field

The basic building block to generate zonal harmonics is a current loop with its central axis lying along the z -direction. A declination angle α is defined with respect to a central point $z = 0$ as shown in Figure 1.31.

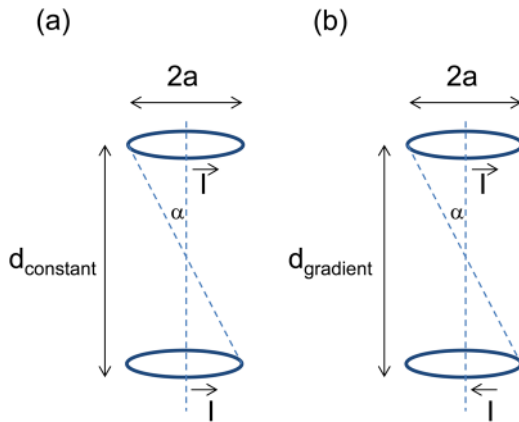


Figure 1.31 Two wire loops producing (a) a constant homogeneous field and (b) a linear gradient. In this case, the declination angle α is solved for using a spherical harmonic approach.

The magnetic field in terms of zonal harmonics is given by:

$$B_z = \frac{\mu_0 I}{2a} \sum_{n=0}^{\infty} \left(\frac{z}{a}\right)^n \sin \alpha P_{n+1,1}(\cos \alpha) \quad (1.70)$$

If a second loop is placed symmetrically about $z = 0$, then one can use the fact that:

$$P_{n+1,1}[\cos(\pi - \alpha)] = (-1)^n P_{n+1,1}[\cos \alpha] \quad (1.71)$$

and if equal currents are applied in the same direction in each loop, then eqn (1.71) means that all the odd zonal terms in z , z^3 , z^5 etc. are cancelled out, leaving the desired term (i.e. the homogeneous magnetic field) in z^0 and the first terms that must be cancelled are in z^2 . From eqn (1.70) the contribution is determined by the value of $P_{3,1}(\cos \alpha)$. Using Table 1.2, this value is zero when $5 \cos^2 \alpha - 1 = 0$, from which $\alpha = 63^\circ$ and $d_{\text{constant}} = a$, i.e. the separation is equal to the radius, the same value (fortunately!) as derived in example A1.

Example B2. Generating a Linear Magnetic Field Gradient in z

Consider the same two loops of wire; if the currents in the two loops are now equal and *opposite*, then even orders cancel, i.e. $z^2 = z^4 = z^6 = 0$. Therefore, the first term that needs to be set to zero is the third order one. From Table 1.2, $P_{4,1}$ contains a term in $(7 \cos^3 \theta - 3 \cos \theta)$, which is equal to zero for $\theta = 49.1^\circ$. This corresponds to a separation given by 1.73 times the radius.

Example B3. Generating a Linear Magnetic Field Gradient in x or y

As can be appreciated from Figure 1.29, generating a magnetic field gradient in either the x - or y -direction involves spherical harmonics with $n = 1$, $m = \pm 1$, and since $m \neq 0$ these involve tesseral harmonics rather than zonal harmonics. Unlike zonal harmonics, tesseral harmonics cannot be generated by a current loop, but can be generated instead using arcs of current, as shown in Figure 1.32(a). As shown by Romeo and Hoult,⁴² the magnetic field produced by such an arc is given by:

$$B = I \sum_{n=0}^{\infty} \sum_{m=0}^n C_{n,m} \frac{r^n}{f^{n+1}} P_{n,m}(\cos \theta) \cos(m\phi - m\psi) d\psi \quad (1.72)$$

where $d\psi$ represents the azimuthal width of the arc. In this case the constant terms $C_{n,m}$ contain two associated Legendre polynomials. As was shown previously for rings, if two arcs are placed 180° apart with current flowing in opposite directions, then the even degrees cancel out, as shown in Figure 1.32(a). So, with respect to the degree n there are terms in B_{11} , B_{13} , B_{15} etc. and

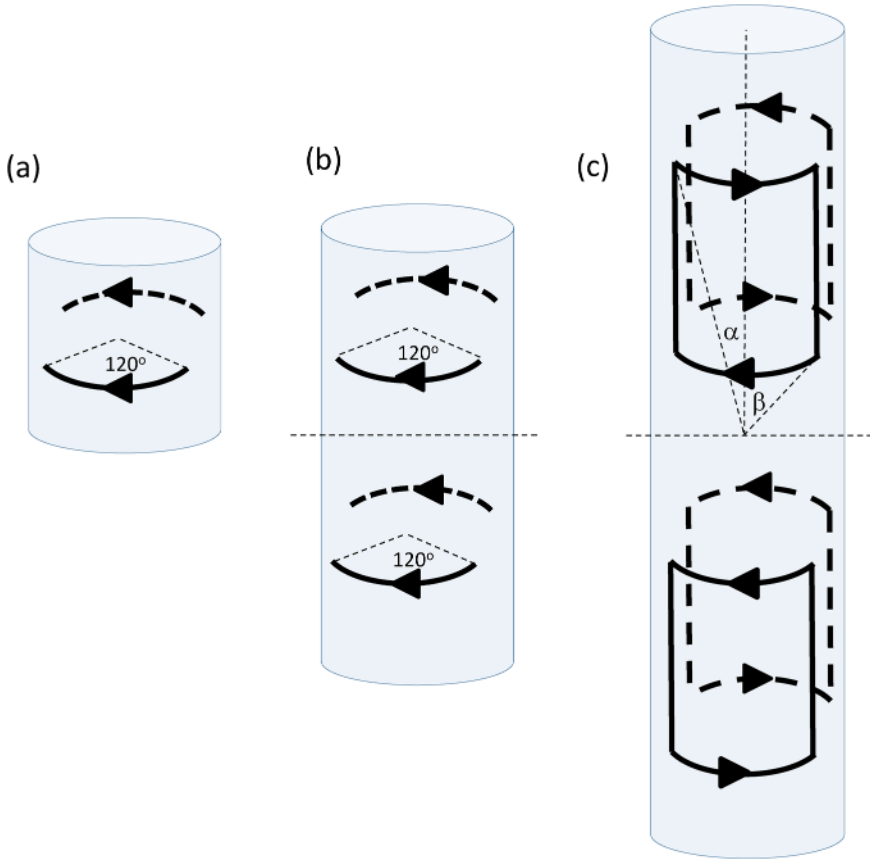


Figure 1.32 (a) An arc of current produces tesseral spherical harmonics. Two arcs placed 180° apart cancel out even degrees of these harmonics (note that the arcs are shown as not being physically connected). The angle 120° is chosen to cancel the B_{13} term. (b) By adding additional arcs symmetrically about the $z = 0$ plane, even orders are cancelled. (c) Physical realization of the gradient coil involves connecting the individual arcs by straight line sections, and optimizing the values of α and β for linearity.

with respect to the order m there are terms in B_{21}, B_{31}, B_{41} etc. The term in B_{13} can be cancelled by appropriate choice of the width $\Delta\psi$ of the arc:

$$B \propto \int_{-\Delta\psi/2}^{\Delta\psi/2} \cos(m\phi - m\psi) d\psi = \frac{2}{m} \cos m\phi \sin\left(\frac{m\Delta\psi}{2}\right) \quad (1.73)$$

This term is zero when the angle subtended by the arc is 120° . The next step is to cancel out the higher order terms. As shown in the previous example, by using a symmetrical arrangement about the $z = 0$ axis, even order terms are cancelled out by extending the number of arcs from two to four, as shown in Figure 1.32(b). The next term is the contribution from B_{31} , which as

also shown in Romeo and Hoult,⁴² can be made equal to zero by calculating the relevant value of $C_{n,m}$ and results in the arrangement shown in Figure 1.32(c), with the values of α and β given by 21.3° and 68.7° , respectively.

References

1. A. Abragam, *The Principles of Nuclear Magnetism*, Clarendon Press, 1961.
2. R. R. Ernst, G. Bodenhausen and A. Wokaun, *Principles of Nuclear Magnetic Resonance in One and Two Dimensions*, Clarendon Press, 1987.
3. A. E. Derome, *Modern NMR Techniques for Chemistry Research*, Pergamon Press, 1993.
4. J. Cavanagh, W. J. Fairbrother, A. G. Palmer, N. J. Skelton and M. Rance, *Protein NMR Spectroscopy, Principles and Practice*, Academic Press, 2010.
5. J. Keeler, *Understanding NMR Spectroscopy*, Wiley-Blackwell, 2010.
6. C. P. Slichter, *Principles of Magnetic Resonance*, Springer, 2010.
7. M. Mehring, *High Resolution NMR Spectroscopy in Solids*, Springer, 2012.
8. M. J. Duer, *Solid State NMR Spectroscopy*, Wiley-Blackwell, 2001.
9. D. C. Apperley, R. K. Harris and P. Hodgkinson, *Solid State NMR: Basic Principles & Practice*, Momentum Press, 2012.
10. P. T. Callaghan, *Principles of Nuclear Magnetic Resonance Microscopy*, Clarendon Press, 1991.
11. Z. P. Liang and P. C. Lauterbur, *Principles of Magnetic Resonance Imaging: A Signal Processing Perspective*, John Wiley & Sons, 1999.
12. M. A. Bernstein, K. F. Z. King and X. J. Zhou, *Handbook of MRI pulse sequences*, Academic Press, 2004.
13. R. W. Brown, Y. C. Cheng, E. M. Haake, M. R. Thompson and R. Venkatesan, *Magnetic Resonance Imaging: Physical Properties and Sequence Design*, Wiley-Blackwell, 2014.
14. F. Bloch, W. W. Hansen and M. Packard, *Phys. Rev.*, 1946, **69**, 127.
15. D. Moskau, *Concepts Magn. Reson.*, 2002, **15**, 164.
16. R. E. Hurd, *J. Magn. Reson.*, 1990, **87**, 422.
17. E. O. Stejskal and J. E. Tanner, *J. Chem. Phys.*, 1965, **42**, 288.
18. G. E. Wesbey, M. E. Moseley and R. L. Ehman, *Invest. Radiol.*, 1984, **19**, 491.
19. P. C. Lauterbur, *Nature*, 1973, **242**, 190.
20. P. Mansfield and P. K. Grannell, *J. Phys. C: Solid State Phys.*, 1973, **6**, L422.
21. P. J. Hajduk, E. T. Olejniczak and S. W. Fesik, *J. Am. Chem. Soc.*, 1997, **119**, 12257.
22. N. Esturau and J. F. Espinosa, *J. Org. Chem.*, 2006, **71**, 4103.
23. C. Beaulieu, H. D'Arceuil, M. Hedehus, A. de Crespigny, A. Kastrup and M. E. Moseley, *Semin. Pediatr. Neurol.*, 1999, **6**, 87.
24. P. J. Basser, J. Mattiello and D. LeBihan, *J. Magn. Reson., Ser. B*, 1994, **103**, 247.
25. J. H. Jensen and J. A. Helpert, *NMR Biomed.*, 2010, **23**, 698.
26. J. H. Jensen, J. A. Helpert, A. Ramani, H. Z. Lu and K. Kaczynski, *Magn. Reson. Med.*, 2005, **53**, 1432.

27. S. Mori, B. J. Crain, V. P. Chacko and P. C. van Zijl, *Ann. Neurol.*, 1999, **45**, 265.
28. J. A. McNab, B. L. Edlow, T. Witzel, S. Y. Huang, H. Bhat, K. Heberlein, T. Feiweier, K. C. Liu, B. Keil, J. Cohen-Adad, M. D. Tisdall, R. D. Folkerth, H. C. Kinney and L. L. Wald, *Neuroimage*, 2013, **80**, 234.
29. K. Setsompop, R. Kimmlingen, E. Eberlein, T. Witzel, J. Cohen-Adad, J. A. McNab, B. Keil, M. D. Tisdall, P. Hoecht, P. Dietz, S. F. Cauley, V. Tountcheva, V. Matschl, V. H. Lenz, K. Heberlein, A. Potthast, H. Thein, J. Van Horn, A. Toga, F. Schmitt, D. Lehne, B. R. Rosen, V. Wedeen and L. L. Wald, *Neuroimage*, 2013, **80**, 220.
30. C. Barmet, N. De Zanche, B. J. Wilm and K. P. Pruessmann, *Magn. Reson. Med.*, 2009, **62**, 269.
31. E. R. Andrew, A. Bradbury and R. G. Eades, *Nature*, 1958, **182**, 1659.
32. L. B. Andreas, T. Le Marchand, K. Jaudzems and G. Pintacuda, *J. Magn. Reson.*, 2015, **253**, 36.
33. U. Haeberle and J. S. Waugh, *Phys. Rev.*, 1968, **175**, 453.
34. P. Mansfield, M. J. Orchard, D. C. Stalker and K. H. Richards, *Phys. Rev. B*, 1973, **7**, 90.
35. W. K. Rhim, D. D. Elleman and R. W. Vaughan, *J. Chem. Phys.*, 1973, **58**, 1772.
36. J. S. Waugh, L. M. Huber and U. Haeberle, *Phys. Rev. Lett.*, 1968, **20**, 180.
37. A. Pines, M. G. Gibby and J. S. Waugh, *J. Chem. Phys.*, 1973, **59**, 569.
38. W. E. Maas, A. Bielecki, M. Ziliox, F. H. Laukien and D. G. Cory, *J. Magn. Reson.*, 1999, **141**, 29.
39. W. E. Maas, F. H. Laukien and D. G. Cory, *J. Am. Chem. Soc.*, 1996, **118**, 13085.
40. D. B. Twieg, *Med. Phys.*, 1983, **10**, 610.
41. S. Ljunggren, *J. Magn. Reson.*, 1983, **54**, 338.
42. F. Romeo and D. I. Hoult, *Magn. Reson. Med.*, 1984, **1**, 44.